Tracking Mesoscale Pressure Perturbations Using the USArray Transportable Array

ALEXANDER A. JACQUES, JOHN D. HOREL, AND ERIK T. CROSMAN

Department of Atmospheric Sciences, University of Utah, Salt Lake City, Utah

FRANK L. VERNON

Scripps Institution of Oceanography, University of California, San Diego, La Jolla, California

ABSTRACT

Mesoscale convective phenomena induce pressure perturbations that can alter the strength and magnitude of surface winds, precipitation, and other sensible weather, which, in some cases, can inflict injuries and damage to property. This work extends prior research to identify and characterize mesoscale pressure features using a unique resource of 1-Hz pressure observations available from the USArray Transportable Array (TA) seismic field campaign.

A two-dimensional variational technique is used to obtain 5-km surface pressure analysis grids every 5 min from 1 March to 31 August 2011 from the TA observations and gridded surface pressure from the Real-Time Mesoscale Analysis over a swath of the central United States. Bandpass-filtering and feature-tracking algorithms are employed to isolate, identify, and assess prominent mesoscale pressure perturbations and their properties. Two case studies, the first involving mesoscale convective systems and the second using a solitary gravity wave, are analyzed using additional surface observation and gridded data resources. Summary statistics for tracked features during the period reviewed indicate a majority of perturbations last less than 3 h, produce maximum perturbation magnitudes between 2 and 5 hPa, and move at speeds ranging from 15 to 35 m s^{-1}. The results of this study combined with improvements nationwide in real-time access to pressure observations at subhourly reporting intervals highlight the potential for improved detection and nowcasting of high-impact mesoscale weather features.

1. Introduction

Many prominent mesoscale phenomena within the troposphere lead to pressure perturbations that can be identified by surface-based sensors after removing diurnal, synoptic, and seasonal-scale fluctuations in the measured time series (e.g., Jacques et al. 2015). Mesoscale processes, such as large-amplitude gravity waves and convective systems, can result in very large pressure perturbations coupled with other surface-based weather impacts. Mesoscale convective systems (MCSs), in particular bow echoes and derechos, are often associated with very strong positive mesoscale perturbations induced by the development and maintenance of a local mesohigh within the system such that the leading edge of the perturbation is often associated with strong damaging winds (Loehrer and Johnson 1995; Evans and Doswell 2001; Engerer et al. 2008; Metz and Bosart 2010). Following the mesohigh, larger MCSs often have a wake low feature typically characterized by a large negative mesoscale pressure perturbation. While typically less potent, occasionally severe winds are generated toward the back of these wake lows as well (Loehrer and Johnson 1995; Coleman and Knupp 2009). Remnant pressure perturbations associated with mesoscale convective vortices can also remain after precipitation and can sometimes serve as initiation points for redevelopment (e.g., Galarneau et al. 2009).

Large-amplitude mesoscale gravity waves, which can originate from a variety of processes and often travel large distances before dissipating (e.g., Achatz et al. 2017), have also been extensively studied and remain difficult to forecast using currently available conventional surface weather observations and numerical

Corresponding author: Alexander A. Jacques, alexander.jacques@utah.edu

guidance. The movement, amplification, and decay of such features through generally stable environments has often been a focus for research (Bosart and Seimon 1988; Crook 1988; Ramamurthy et al. 1993; Zhang et al. 2001; Plougonven and Zhang 2014). Additionally, their impacts on precipitation generation or suppression (Mapes 1993; Bosart et al. 1998), wind field amplification or modification (Bosart and Seimon 1988; Schneider 1990), and convection initiation (Ruppert and Bosart 2014) have also been examined, mainly through analysis of case events that had large impacts.

A suite of observational and numerical resources have been used to identify and categorize mesoscale weather features that produce large pressure fluctuations. In many cases, detailed analyses of perturbation pressure fields have focused on specific cases. Several studies have used time series analysis techniques including frequency filtering (Koch and O'Handley 1997; Koch and Saleeby 2001; Adams-Selin and Johnson 2010; Jacques et al. 2015) and wavelet analysis (Grivet-Talocia and Einaudi 1998; Grivet-Talocia et al. 1999) to isolate the specific pressure perturbation features. Other studies have taken more holistic approaches to produce regional climatologies of prominent mesoscale feature occurrences (e.g., Koppel et al. 2000; Bentley et al. 2000; Guastini and Bosart 2016). Phase speeds for features such as MCS and inertial gravity waves have been estimated to be typically within $15-35\,\mathrm{m\,s^{-1}}$ (Koppel et al. 2000). However, cases have also been documented involving gravity waves that have moved near or above the upper bound of $35\,\mathrm{m\,s^{-1}}$ (Bosart et al. 1998; Adams-Selin and Johnson 2013).

Several of the preceding existing mesoscale feature climatologies have relied upon subjective analysis to identify unique characteristics that describe the particular feature of interest. However, objective feature identification and tracking has also been utilized to identify and track synoptic-scale features (König et al. 1993; Hodges 1994; Hoskins and Hodges 2002; Hodges et al. 2003; Raible et al. 2008; Kravtsov et al. 2015). Techniques such as the Storm Cell Identification and Tracking (SCIT; Johnson et al. 1998), Tornado Vortex Signature (TVS; Brown and Wood 2012), and cloud-tracking algorithms (e.g., Liu et al. 2014) have been employed to identify smaller features. The Method for Object-Based Diagnostic Evaluation (MODE) has been a prominent tool for numerical weather prediction forecast verification (Davis et al. 2006, 2009). An extension known as MODE Time Domain (MODE-TD) incorporates the ability to follow a detected feature over time and assess properties such as speed and direction, in addition to nontemporal properties such as areal extent (Bullock 2011). Both have been utilized for verification of mesoscale features in many studies (Bullock 2011; Mittermaier and Bullock 2013; Clark et al. 2014; McMillen and Steenburgh 2015).

Pressure observations have been a prominent resource to initialize global and mesoscale forecast models (Anderson et al. 2005; Lei and Anderson 2014; Madaus et al. 2014; Ingleby 2015; Centurioni et al. 2017). Numerical reanalysis projects, including the twentieth-century reanalysis project, have also utilized archived pressure observations to provide more accurate representation of prior high-impact events (Whitaker et al. 2004; Compo et al. 2006, 2011). Lacking potential representativeness errors of many other state variables, pressure data from diverse resources such as unconventional mesonets (Horel et al. 2002) and mobile phones (Mass and Madaus 2014) are more amenable for operational data assimilation.

A unique resource of high temporal resolution pressure observations from the EarthScope USArray Transportable Array (TA) is used in this study. The TA, described further by Tytell et al. (2016), is part of a National Science Foundation geoscience field campaign and involved over 400 surface-based instrument platforms deployed in a Cartesian-type fashion (~70-km spacing) across a section of the continental United States (CONUS). The design and deployment strategy of the TA provided geoscientists with a detailed dataset of the North American continent subsurface (Tytell et al. 2016). Atmospheric pressure sensors, reporting at 1 and 40 Hz, were installed in late 2009 while the TA was located over the central CONUS to aid in identifying signals in seismic observations induced by nonseismic phenomena (de Groot-Hedlin et al. 2008; Hedlin et al. 2010, 2012; de Groot-Hedlin et al. 2014).

Jacques et al. (2016) describe the TA pressure data in greater detail and their ongoing archival for the CONUS and Alaska in the Research Data Archive at the National Center for Atmospheric Research. Time series for every available station were analyzed during the period between 1 January 2010 and 28 February 2014 by Jacques et al. (2015) to assess mesoscale (10 min–4 h), subsynoptic (4–30 h), and synoptic (30 h–5 day) pressure fluctuations as a function of geographic location and season. A prominent region of mesoscale pressure perturbation activity was noted across the central portion of the CONUS during the spring (MAM) and summer (JJA) months, consistent with past reviews of MCS and gravity wave events. However, since each time series was analyzed independently, it was not possible to characterize spatial and movement characteristics of pressure features rippling across the region where the TA was installed.
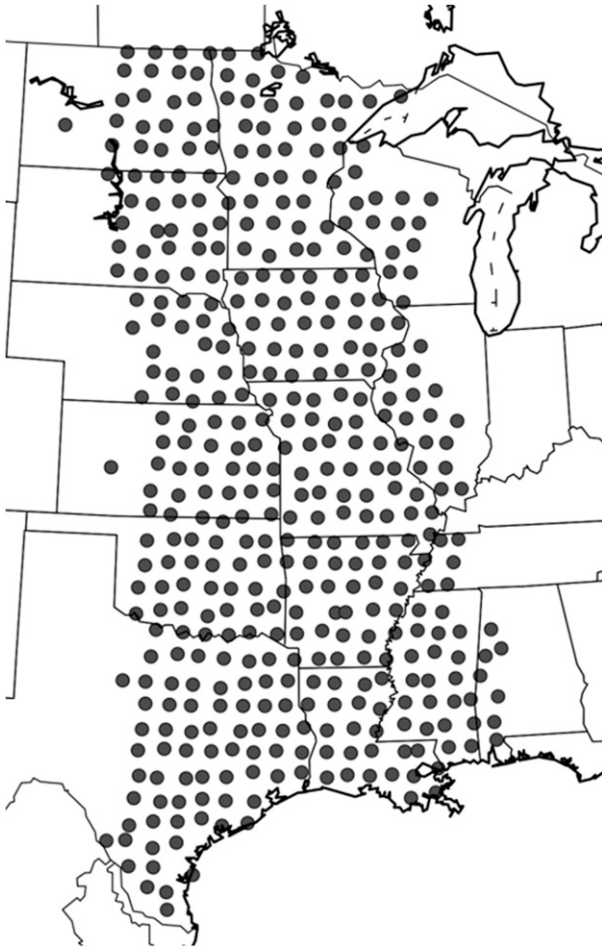
FIG. 1. Locations of TA platforms with pressure observations during 1 Mar 2011–31 Aug 2011.

This study extends the work conducted by Jacques et al. (2015) to identify, track, and characterize pressure features during a period of prominent mesoscale activity over the TA domain (1 March–31 August 2011). Figure 1 illustrates the TA deployment during this period in a north–south swath within the central CONUS, stretching from the Canadian border south to the western Gulf of Mexico coastline. Section 2 depicts the methods used to combine the TA observations with numerical grids of surface pressure data to produce a dataset with adequate spatial (5 km) and temporal (5 min) resolution to detect prominent mesoscale pressure perturbations. Section 2 also describes the methodology used to filter the analysis datasets for mesoscale perturbations as well as the detection algorithm developed to extract the pressure features. Features that can be tracked for at least an hour and have areal extents greater than $10\,000\,\mathrm{km}^2$ are assessed. Section 3 presents two contrasting cases during the period of interest. Section 4 summarizes the detected mesoscale features in

terms of their location, size, phenomena type, magnitude, phase speed, and direction. Section 5 summarizes the results and discusses how this work might be extended operationally to detect and nowcast high-impact mesoscale weather features.

2. Data and methods

a. Pressure data resources

1) TA OBSERVATIONS

As described by Tytell et al. (2016), pressure sensors such as the Setra-278 pressure transducer were installed within a subsurface TA vault with tubing extending up to the surface. Data from the Setra-278 sensors were recorded and available at interval rates of 1 and 40 Hz. Jacques et al. (2016) describe the methods used to collect the data from the Incorporated Research Institutions for Seismology (IRIS) systems and archive them in an efficient format for atmospheric applications. The data are archived from 1 January 2010–31 December 2015 in the Research Data Archive at the National Center for Atmospheric Research, with plans to continue updating the archive annually until the completion of the project. The pressure observations can also be visualized via the web (http://meso1.chpc.utah.edu/usarray; Jacques et al. 2015).

The relatively short-term (~2 yr) deployment strategy for most TA sites inhibits their use for long-term studies. However, advantages for using TA observations for this study include their temporal resolution, sensor uniformity, deployment strategy, and data quality. The 1-Hz observations from the Setra-278 sensors were resampled at 5-min intervals for this work. The Cartesian-like (~70 km) spacing of the 400 sensors is unique compared to conventional and other observation networks that tend to be clustered in urban areas (Tyndall and Horel 2013). Jacques et al. (2015) summarize the objective rate-of-change thresholds of $2\,\mathrm{hPa\,s}^{-1}$ and $2\,\mathrm{hPa}$ min^{-1} used to indicate suspect periods of data for each TA site, which are flagged after review. Sensor performance for the TA general from 1 January 2010 to 31 December 2015 is very high, with a median 99.79% uptime per site (Jacques et al. 2016).

2) BACKGROUND GRIDS

The Real-Time Mesoscale Analysis (RTMA) product of the National Centers for Environmental Prediction (NCEP) is used to obtain hourly surface pressure data on a regular 5-km horizontal grid during 2011 (de Pondeca et al. 2011). The 2011 RTMA used downscaled 1-h surface pressure forecasts from the Rapid Update Cycle
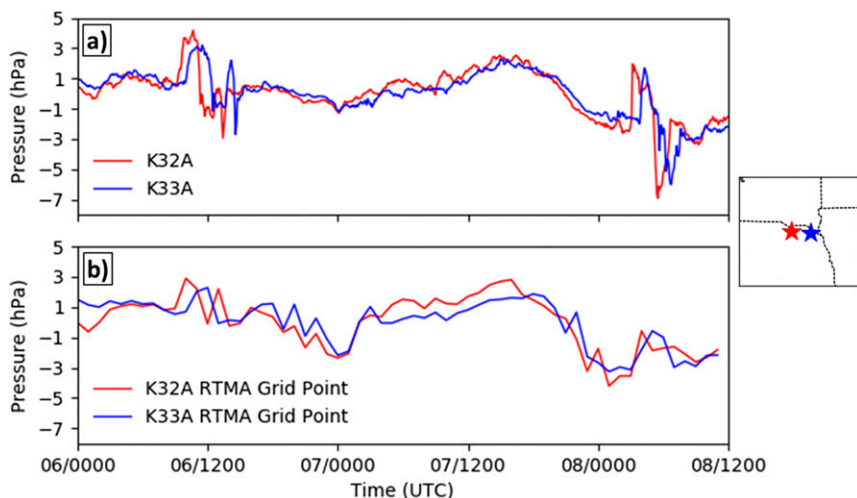
FIG. 2. Pressure during the period 0000 UTC 6 Aug–1200 UTC 8 Aug 2011 from (a) TA 5-min observations at stations K32A (red) and K33A (blue) in northeastern Nebraska shown as colored markers on map to the right and (b) the RTMA hourly background gridpoint values closest to those locations. The mean pressures over this period were removed from their respective time series.

(RUC) model as its background and then performed a univariate two-dimensional variational analysis to incorporate thousands of pressure observations over the CONUS (Benjamin et al. 2007). Since TA observations were not made available to NCEP until March 2012, TA observations from 2011 were not incorporated into the RTMA analyses and hence represent an independent dataset.

Visual inspection of the hourly RTMA pressure fields in our region of interest indicated many nonphysical mesoscale-appearing pressure features. These features likely arise from the combined effects of observational errors, inaccurate station elevation metadata leading to errors in the reduction of surface pressure to sea level pressure, differences from one hour to the next in what pressure observations are available, and poorly resolved features in the RUC background grids. Figure 2 contrasts the 5-min pressure time series from two adjacent TA stations (K32A and K33A) in northeastern Nebraska to the RTMA hourly time series available at those locations from 0000 UTC 6 August–1200 UTC 8 August 2011. Superimposed on longer time-scale pressure changes are two distinct pressure features arising from convective systems moving from west (K32A) to east (K33A) in the time periods 0600–1800 UTC 6 August and 0200–0900 UTC 12 August 2011. While the RTMA captures the longer time-scale pressure variations quite well, the two observed mesoscale events are not well defined by the RTMA and considerable "noise" (hour to hour variations approaching 2 hPa) is evident at these locations. To reduce the impacts of the described

errors, a Butterworth low-pass ($\geq$12 h) temporal filter was applied to the hourly RTMA surface pressure grids. This filter helps to retain the temporal and spatial evolution of large-scale weather features such as those evident in Fig. 2b. The present mesoscale features then remain observable by utilizing the TA observations (e.g., Fig. 2a).

b. Pressure tendency analyses

The enhanced temporal resolution of the TA observations is not sufficient to overcome the inherent limits of the relatively coarse distance ($\sim$70 km) between sensors to detect and track mesoscale pressure features, unless the features are traveling in a quasi-linear fashion from one site to another. Similarly, even if the RTMA pressure fields at 5-km resolution did not suffer during 2011 from apparent errors, the hourly temporal resolution of those grids inhibits establishing temporal continuity for individual pressure features as many often develop, grow, and decay in close proximity to one another. Hence, as an approach to take full advantage of the resources available, we adjust the relatively high spatial resolution of the RTMA background grids with the high temporal resolution of the TA observations. As a further precaution to reduce errors arising from mismatches between the gridded elevations and those of the TA sites, our analyses are derived from gridded values and observations converted from surface pressure to 5-min pressure tendency, a step that has been used in data assimilation and other similar studies (e.g., Madaus et al. 2014).

The University of Utah Two-Dimensional Variational Analysis (UU2DVAR; Tyndall and Horel 2013) is used to generate pressure tendency analyses every 5 min on the 5-km grid of the RTMA background fields. The hourly RTMA grids are interpolated to 5-min intervals using cubic splines over the entire 6-month period at each grid point in order to match the temporal resolution of the TA observations. The background to observation error variance ratio was specified a priori to be 1.0, which implies that the two data sources (RTMA and TA observations) are assumed to be equally credible. After initial testing, the background error covariances are assumed as well to decay isotropically as a function of the distance between the grid points with an e-folding decorrelation length scale of 80 km. Since the average spacing between TA sites is roughly similar, it is implied that innovations (differences between the observations and background values) at multiple nearby locations will influence the analysis at any particular grid point.

Pressure tendency analysis grids are then converted back to surface pressure using the analysis from 5 min prior (with the exception of the first analysis, which utilized the original background RTMA grid), and then reduced to sea level via the altimeter setting formula in order to better visualize the pressure fields in the presence of topography. Background (Fig. 3b), analysis (Fig. 3c), and the difference between the two grids (Fig. 3d) highlight how the 5-min TA observations (Fig. 3a) help detect mesoscale pressure features that would not be evident on the basis of the RTMA background fields alone.

c. Feature identification and tracking

To isolate mesoscale pressure features, a Butterworth bandpass filter with temporal bounds corresponding to 10 min and 12 h is applied to surface pressure time series at every analysis grid point to produce grids of mesoscale pressure perturbations at 5-min intervals. These filter bounds were selected to include multiple scales of mesoscale pressure perturbation features while reducing impacts from diurnal and synoptic pressure variations. Mesoscale features are first identified on each independent analysis grid. Regions of mesoscale activity are identified as areas of conjoined grid cells where a pressure perturbation larger than 1 hPa in absolute magnitude was detected. Attributes, including the areal extent of the 1-hPa absolute magnitude region, are calculated for each identified perturbation.

To begin the process of matching identified perturbations across time, procedures often used to verify features embedded within numerical forecasts (e.g., Clark et al. 2014) are utilized. An iterative approach is used to track detected features over successive analysis grids that allow features to form, merge, and decay over extended periods. Mesoscale features are defined here as those with an absolute perturbation magnitude of at least 1 hPa, detected for at least 1 h, and with an areal extent of at least 10 000 km^2 (radial dimension of ~100 km) at some point during their existence. These thresholds provide opportunity for the feature to be assessed by at least one hourly RTMA background grid and by potentially several TA stations. Given the scales of interest and propagation speeds (15–35 m s^{-1}) of pressure perturbations often associated with high-impact weather, it is to be expected that a propagating feature overlaps within a relatively large region on the 5-km grid within a 20-min window. Hence, temporal matching is first conducted using analysis grids separated by 5 min and then overlapping features over longer temporal ranges (10, 15, and 20 min apart) are matched in a fashion similar to the spatiotemporal overlap approaches that have been used in feature detection algorithms for both radar (e.g., Johnson et al. 1998; Jung and Lee 2015) and MODE-TD (e.g., Bullock 2011; Clark et al. 2014). To manage as best as possible splitting and merging of features, the centroid distance to the location of maximum magnitude of a feature is utilized as a means to determine those features that continue, form, or dissipate as well as allow for features that occasionally fall below the 1-hPa threshold for a short period within their lifetime but are clearly the same feature previously discovered. Subjective reviews with ancillary datasets were conducted to address occasional situations where merging and splitting features appeared to be unphysical. Such features were rare in occurrence and usually were the result of strong frontal passages with rapidly developing or dissipating convective segments.

Metrics for each feature (e.g., geographic centroid position, maximum absolute magnitude position, maximum absolute perturbation magnitude, etc.) are saved at each 5-min interval of its detected existence. An adaptation of the methodology used by MODE-TD is applied to determine feature speed and direction at each time step within its lifetime. The MODE-TD tool derives the components of zonal (u) and meridional (v) velocity over a feature's lifetime through linear regression using all x- and y-coordinate locations, respectively (Bullock 2011). A similar linear regression is performed here to determine its speed and direction at each time, but the sample is restricted to the positions of the feature within a moving 30-min window around the selected time. This method permits changes in the direction and speed of features, which is often seen with mesoscale systems that move large distances and through varying environments.
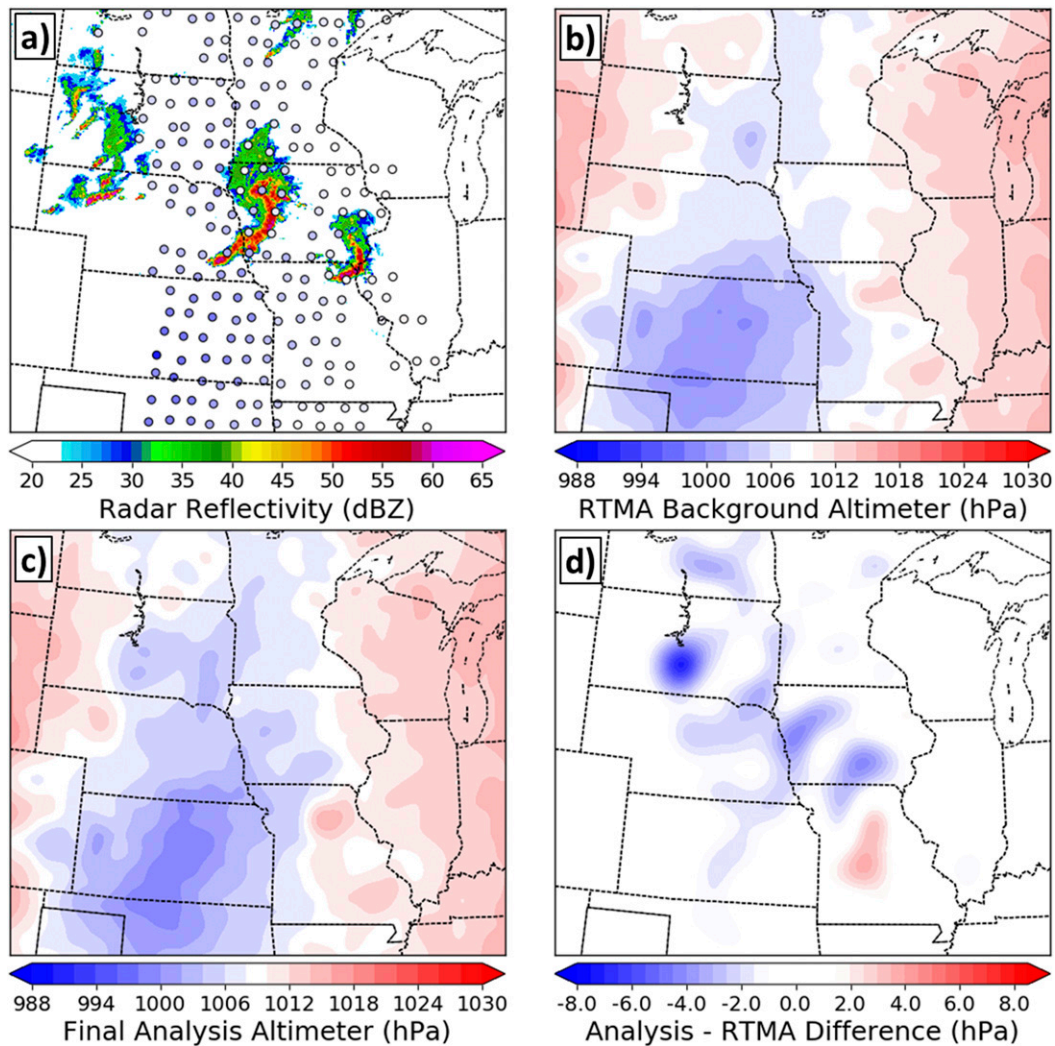
FIG. 3. (a) Radar reflectivity and TA altimeter setting observations, (b) RTMA background grid altimeter, (c) UU2DVAR final analysis altimeter, and (d) the difference between the final analysis and RTMA background for 0200 UTC 27 Jun 2011. Altimeter values were calculated by converting from surface pressure using elevation data for the TA sites and gridded products. Station coloring in (a) is equivalent to the color bars of (b) and (c). Radar reflectivity image courtesy of the Iowa Environmental Mesonet web services.

3. Case studies

a. Event overviews

To demonstrate our approach to identify and track large mesoscale pressure perturbation features, two cases are chosen within the 1 March–31 August 2011 period. Because of the north–south orientation of the TA deployment, the two cases have phenomena with a substantive meridional propagation component so they can be assessed across the TA domain for longer periods of time. The first case involves the development and movement of two successive MCS complexes that formed overnight on 11 August 2011 over the northern and central Great Plains. The second case involves a mesoscale

gravity wave that formed in association with a synoptic system on 27 April 2011 and propagated northward away from the system.

b. 11–12 August 2011 successive northern plains MCS events

1) SYNOPSIS

The analysis for this case focuses on two semi-linear convective complexes that initially formed over South Dakota and moved to the southeast over several hours into Nebraska and western Iowa before continuing southeast at varying intensities into northeast Kansas and northwest Missouri. NARR analysis at 1800 UTC 11 August 2011, a
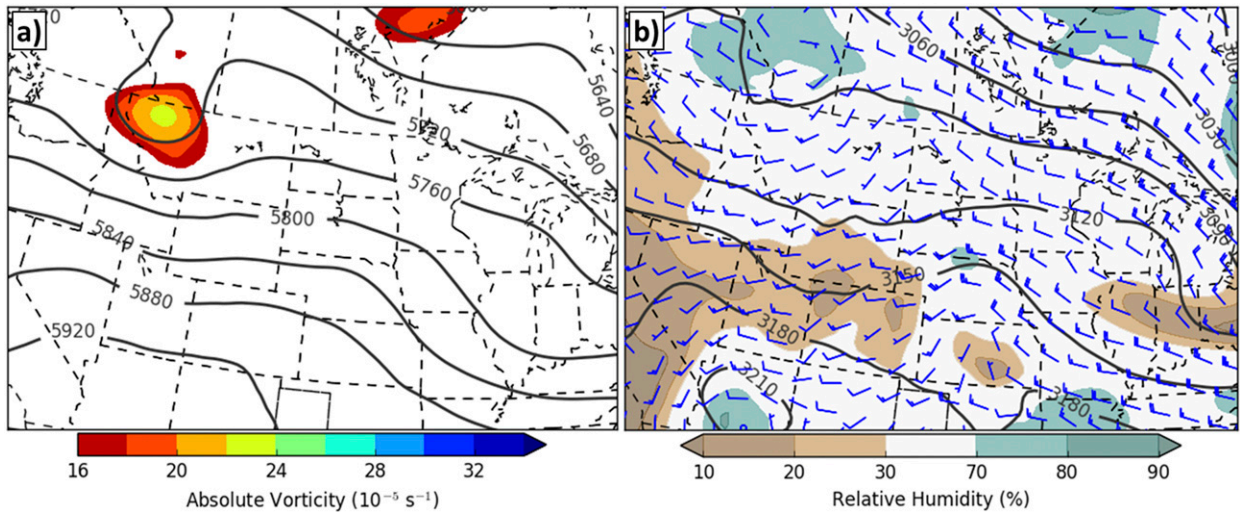
FIG. 4. North American Regional Reanalysis (NARR) valid at 1800 UTC 11 Aug 2011. (a) The 500-hPa geopotential height (solid gray contoured every 40 gpm) and absolute vorticity (shaded according to the scale at the bottom). (b) The 700-hPa geopotential height (solid contoured every 30 gpm), relative humidity (shaded), and wind barbs (full barb 5 m s^{-1}).

few hours prior to the organization of the first MCS, shows midlevel geostrophic flow at 500 (Fig. 4a) and 700 (Fig. 4b) hPa from west to northwest across the central to northern Great Plains. A digging shortwave trough was propagating into Montana at this time as well (Fig. 4a). Figure 5 depicts air temperature, dewpoint, and wind observations from surface-based National Weather Service (NWS) Automated Surface and Weather Observing System (ASOS/AWOS) and Bureau of Land Management Remote Automated Weather Station (RAWS) platforms at 1800 UTC 11 August 2011 obtained from Mesowest (Horel et al. 2002). A warm, moist low-level environment is evident with southerly surface flow across much of eastern and central Nebraska and South Dakota with temperatures ≥ 25°C and high dewpoints ≥ 16°C.

The 0000 UTC 12 August 2011 atmospheric soundings from Aberdeen, South Dakota (Fig. 6a), and North Platte, Nebraska (Fig. 6b), show elevated convective available potential energy (CAPE) values. Both soundings also exhibit the presence of low- to midlevel wind shear supporting the development of organized multicellular structures as well as drier midlevels (600–700 hPa) that support enhanced downdrafts (e.g., Coniglio et al. 2011). Perhaps most noticeable is the presence of a strong low-level capping inversion in Fig. 6b, which likely prevented any surface-based convective development upstream of the first complex.

2) FEATURE ANALYSIS

The first MCS initially forms over central South Dakota and then organizes and moves southeastward into the western periphery of the deployed TA. By 0100 UTC

12 August 2011, the complex forms a classic bow echo structure (Fig. 7a). A region of positive mesoscale pressure perturbations lies near the apex of the bow echo, where the expected mesohigh would reside, and several TA stations, including J32A (Parkston, South Dakota), experience large positive mesoscale pressure perturbations (Fig. 8a).

By 0400 UTC (Fig. 7b), the first MCS and associated mesohigh has rapidly expanded in areal extent. The dashed red line shows the general movement of the feature during its lifetime based on the approach described in section 2. The median speed for this assessed mesohigh feature is 22.4 m s^{-1} in a generally southeast direction. The wake low feature is detected initially at 0400 UTC associated with the northern mesovortex that developed as a part of this MCS (Fig. 7b). Large negative pressure perturbations are recorded at TA stations such as H33A near Clear Lake, South Dakota (Fig. 8b). Initial generation of the second MCS can also begin to be detected at 0400 UTC in South Dakota west of the TA deployment.

The first MCS continues moving south-southeastward and by 0900 UTC lies over northeastern Kansas and northwest Missouri, with a large positive mesoscale pressure perturbation remaining intact. The bow echo initially appears to split with the eastern edge of the bow echo significantly weakening while the southern and southwestern edges of the complex continue to maintain strength. The weakened portion of the MCS can still be seen in the radar reflectivity over southern Minnesota at 0900 UTC (Fig. 7c), though the region of positive mesoscale pressure perturbations has weakened, as shown
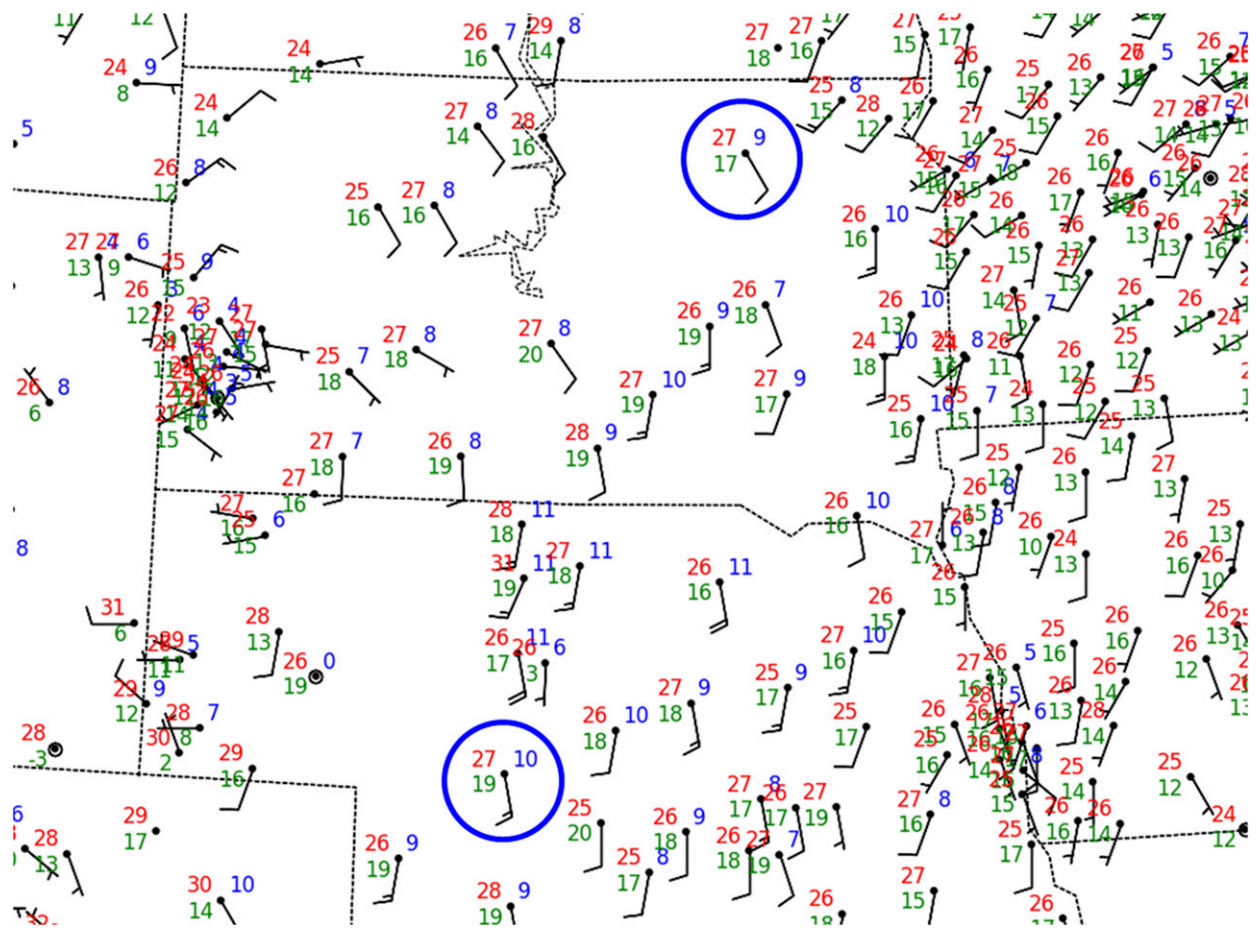
FIG. 5. Selected surface observations at 1800 UTC 11 Aug 2011 over South Dakota and Nebraska. Station plots depict surface temperature (°C, red), dewpoint (°C, green), wind barbs (full barb 5 m s^{-1}), and peak wind gust (m s^{-1}, blue) recorded within an hour of the valid time. Blue circles denote the two sounding locations in Fig. 6.

by the TA observations. The remaining prominent mesohigh region instead shifted southwest to accompany the stronger convection associated with the western portion of the original complex. The western edges of the complex have begun to weaken as well, but the positive mesoscale pressure perturbation remains intact along the general outflow boundary of the complex as seen in Fig. 7c. Further, a wake low feature is well established behind the first MCS, as indicated by a collocated track (blue dashed line) behind the mesohigh track (red dashed line) with a similar median speed of 22.1 m s^{-1}. The second MCS has also formed and is beginning to move into the bounds of the TA domain.

The large mesohigh region with the first MCS dissipates and is no longer detected by 1200 UTC (Fig. 7d). The negative pressure perturbation associated with the trailing wake low region remains intact. The positive perturbation associated with the second complex expands in coverage as the system propagates farther into

the TA domain with a median speed of 20.8 m s^{-1}. This complex remains less organized than the first, with a smaller leading line of convection and larger stratiform region remaining farther back over much of eastern Nebraska. Stations K32A and M33A in northeast and east-central Nebraska, respectively, show the passage of the first MCS mesohigh, wake low, and second complex mesohigh structures quite well via time series of pressure perturbation observations (Figs. 8c,d). NWS and RAWS surface wind observations report wind gusts for both complexes that were approaching, if not surpassing, NWS severe wind criteria of 25.9 m s^{-1}. A peak wind gust of 24 m s^{-1} was recorded at ASOS station KODX (Ord, Nebraska) along the southwestern edge of the leading convective line. An equally intense 24 m s^{-1} wind gust from the east was also recorded by ASOS station KBKX (Brookings Municipal Airport, South Dakota) in association with the wake low of the first MCS. The second complex produced near-severe wind speeds as well with ASOS site KLNK (Lincoln Municipal
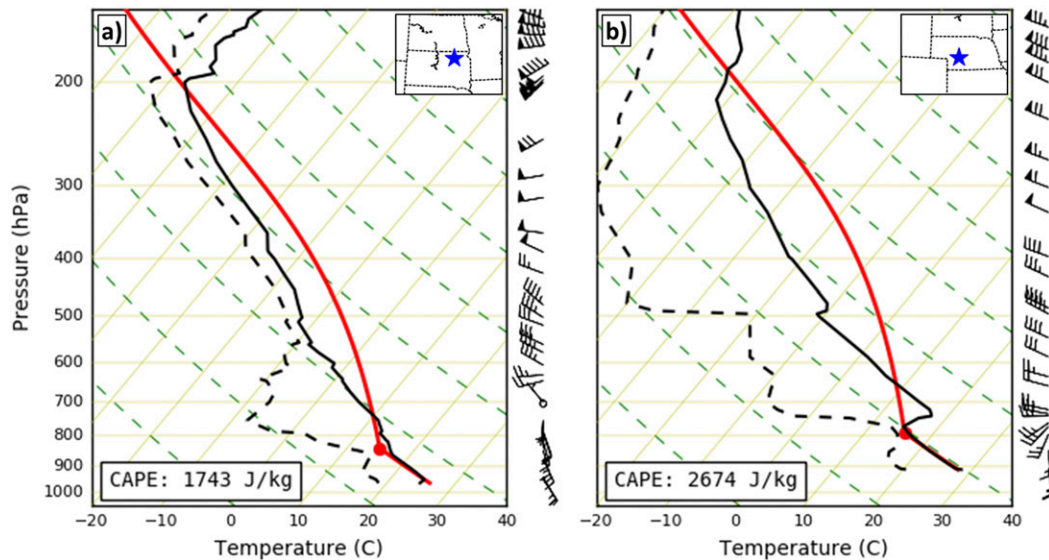
FIG. 6. Skew T–log$p$ diagrams from (a) Aberdeen, South Dakota, and (b) North Platte, Nebraska, at 0000 UTC 12 Aug 2011. Solid (dashed) black lines denote temperature (dewpoint) profiles with observed winds provided to the right of the plot (full barb $5 \, \mathrm{m \, s^{-1}}$). Hypothetical parcel trajectory annotated as red solid line with calculated CAPE in bottom-left text box. Sounding geographic location shown with blue star on inset geographic map.

Airport, Nebraska) recording a $24 \, \mathrm{m \, s^{-1}}$ peak wind gust (not shown).

c. 26–27 April 2011 propagating mesoscale gravity wave

1) SYNOPSIS

The second case involves the development of a mesoscale gravity wave across the south-central CONUS that propagated northward through a large swath of the TA domain early (0000–0600 UTC) 27 April 2011 (de Groot-Hedlin et al. 2014). As will be shown later, the wave originated as a strong negative pressure perturbation across southeast Oklahoma (Fig. 10b) and moved northward through the central Great Plains as a fairly intense negative pressure perturbation, where it was detected well by the TA stations. The wave maintained amplitude until reaching the northern portion of the Great Plains, where it then began to dissipate.

The general synoptic environment that was present during the generation of this feature has been reviewed extensively, as the feature occurred just prior to an extremely devastating and deadly tornado outbreak across Alabama and the surrounding states later on 27 April 2011 (Knupp et al. 2014; Yussouf et al. 2015). The generation point of the mesoscale feature was to the northeast of a developing surface cyclone over northeastern Texas, placing the feature in a synoptic environment that was likely favorable for gravity wave amplification and maintenance. Knupp et al. (2014) provide an in-depth analysis

of the upper-level environment associated with the warm sector of the synoptic system. Figure 9 complements their study by showing soundings for the sector within which the gravity wave traversed. The 0000 UTC 27 April 2011 sounding at Springfield, Missouri, indicates an inversion layer between 900 and 800 hPa, with weaker stability aloft from 800 to 600 hPa (Fig. 9a). Winds within the inversion layer were generally light, while above the inversion layer strong south-southwesterly flow can be seen. Farther north at Topeka, Kansas (Fig. 9b), the inversion layer is higher (based just below 800 hPa) and sharper but remained surmounted by a layer of weaker stability above. The Omaha, Nebraska, sounding (Fig. 9c) depicts an inversion layer beginning just below 750 hPa with a layer of weaker stability above the inversion. Finally, the 0000 UTC sounding recorded at Chanhassen, Minnesota, does not have a sharp inversion layer present, with northeasterly flow backing to northwesterly dominating the lower and midlevels (Fig. 9d). Vertical plots of Brunt–Väisälä frequency for the four soundings indicated values of 0.03–$0.06 \, \mathrm{s^{-1}}$ within the inversion layers described above, with values closer to $0.01 \, \mathrm{s^{-1}}$ above those layers (not shown).

Previous authors (Lindzen and Tung 1976; Bosart et al. 1998; Ruppert and Bosart 2014) have described how the combination of a strong stable inversion layer with a critical level above it in a layer of weaker stability can lead to the trapping and ducting of vertically propagating gravity waves. Figure 10 illustrates the general northerly movement of the negative pressure perturbation associated with the gravity wave (blue contoured region and
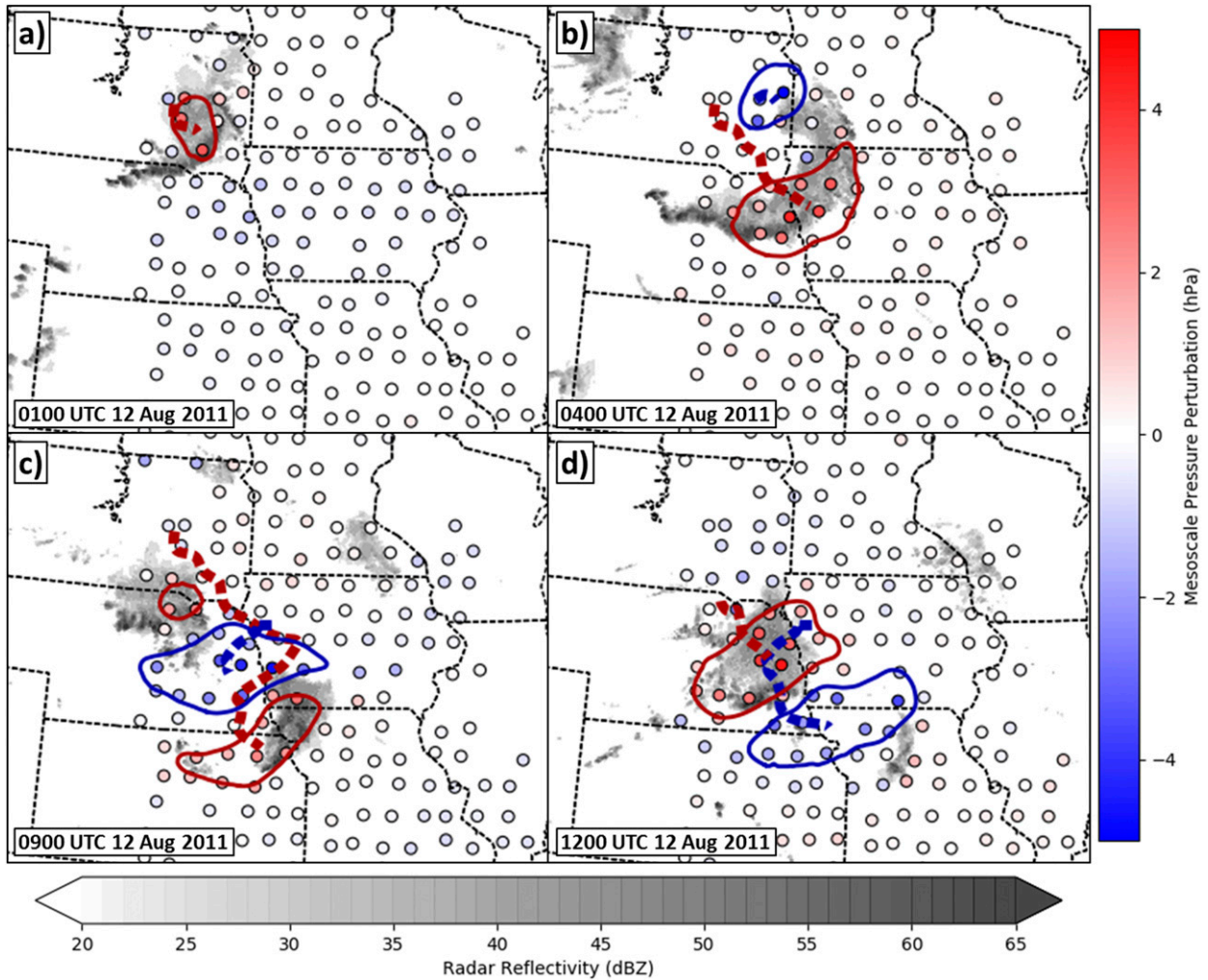
FIG. 7. Pressure perturbation features at (a) 0100, (b) 0400, (c) 0900, and (d) 1200 UTC 12 Aug 2011 over the north-central CONUS. Perturbation features at the selected times are shown as dark red (blue) 1-hPa perturbation contours for positive (negative) magnitudes. Perturbation feature tracks are shown by dashed dark red (blue) lines. Base radar reflectivity > 20 dBZ shaded according to the scale at the bottom.

blue dashed feature track). Reviewing the sounding winds, flow within the layer above the inversion has a large zonal component as opposed to meridional at Topeka and Omaha (Figs. 9b,c), resulting in very low magnitudes of flow component in the direction of wave propagation. This may have aided in the development of a critical level that could maintain wave amplitude as the feature moved northward. Since the Chanhassen sounding (Fig. 9d) has opposing flow without a strong inversion layer, the wave likely dissipated as it continued to move north into Minnesota.

2) PERTURBATION FEATURE ANALYSIS

Convective initiation within the warm sector of the synoptic system begins around 2000 UTC 26 April 2011 in southern Arkansas, as seen on radar imagery (Fig. 10a).

By 2200 UTC (Fig. 10b) convection continues to develop near a surface boundary structure located near Arkansas, southeastern Oklahoma, and northeastern Texas. Co-incident with the convective initiation was the generation of a large negative mesoscale pressure perturbation in southeastern Oklahoma, signifying the birth of the mesoscale gravity wave. It is unclear whether this perturbation was responsible for the convective initiation or vice versa, as described in previous cases (e.g., Bosart et al. 1998). The gravity wave expands and moves north through much of the TA across eastern Kansas, Missouri, and into Iowa from 0000 to 0400 UTC 27 April 2011 (Figs. 10c–e). Precipitation is not associated with this northward-moving feature compared to other stronger gravity wave cases that are either coupled with convection or have modified precipitation distributions
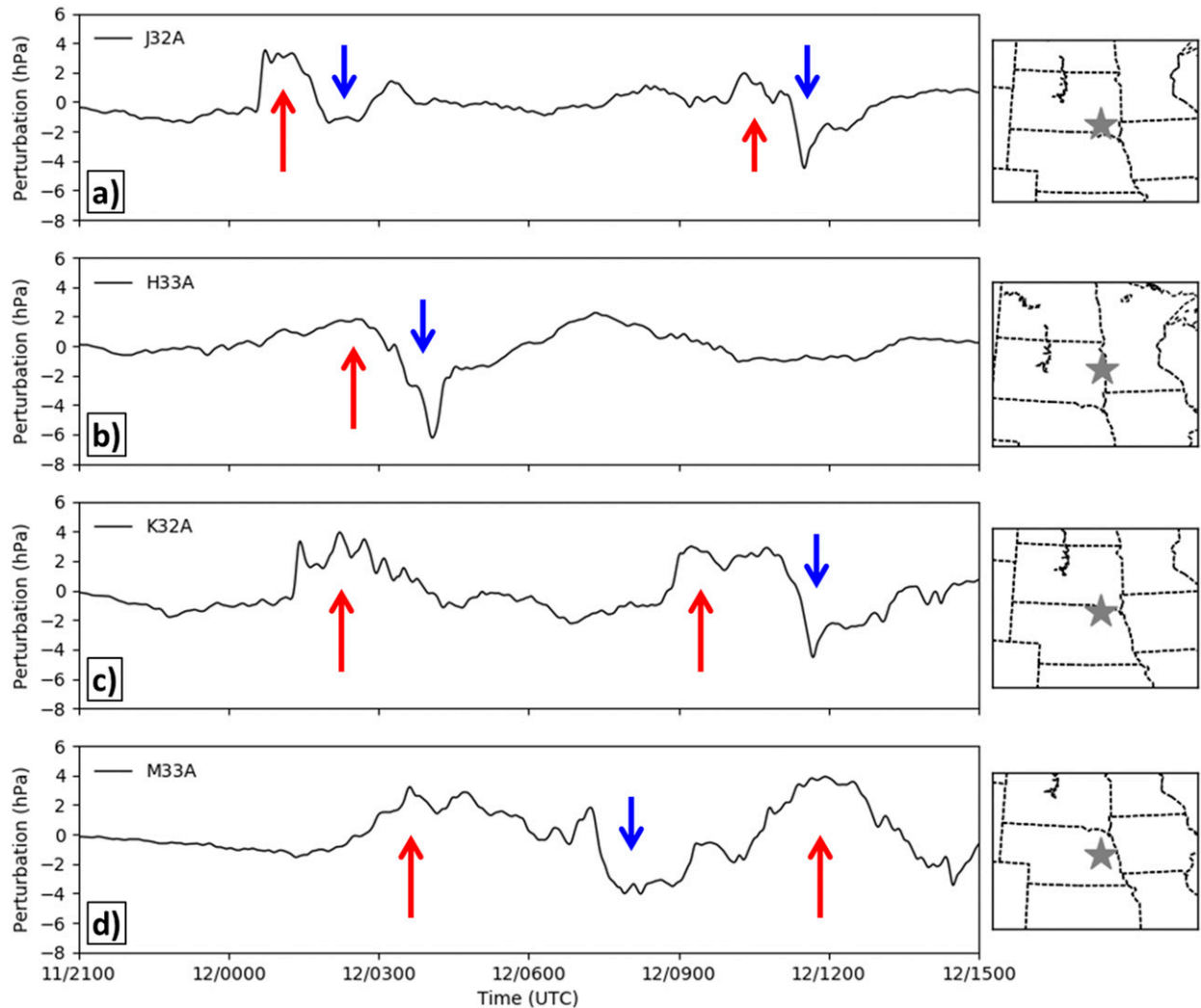
FIG. 8. Pressure perturbations from 2100 UTC 11 Aug 2011–1500 UTC 12 Aug 2011 at TA stations (a) J32A, (b) H33A, (c) K32A, and (d) M33A. Location of stations shown as gray stars on the maps to the right of the time series. Red (blue) arrows denote the passage of mesohighs (wake lows) at various stations, as described in the text.

(e.g., Ruppert and Bosart 2014; Jacques et al. 2015). This feature moves rather quickly, with a median speed of 36.6 m s^{-1}. By 0600 UTC, the feature begins to dissipate as it moves into Minnesota (Fig. 10f).

Pressure perturbation time series at several TA sites along the path of the gravity wave depict the negative mesoscale perturbation experienced as the wave passes (Fig. 11). TA station P36A northwest of Atchison, Kansas, depicts the sharpest pressure decrease associated with the wave (Fig. 11a), with subsequent TA stations farther north (Figs. 11b–d) showing the sharpness of the pressure fall and overall wave amplitude decreasing, implying weakening of the feature over time.

The gravity wave was not intense enough to produce any wind damage impacts, although surface winds were modified as the wave propagated northward (not shown).

For this event, wave passage is coincident with an enhancement of north-northwesterly winds as it translated north, followed by a relaxing of wind speeds behind the gravity wave. In some cases the winds relaxed from 5 to 8 m s^{-1} during the gravity wave passage to near-calm conditions one hour later. The wave did move through a region of the CONUS where wind turbines are abundant, thus identification and tracking of these features have potential applications within the wind energy industry for identification of possible wind ramps.

4. Summary statistics

a. Feature occurrences

As mentioned in section 2, mesoscale pressure perturbation features are defined here to last at least 1 h and
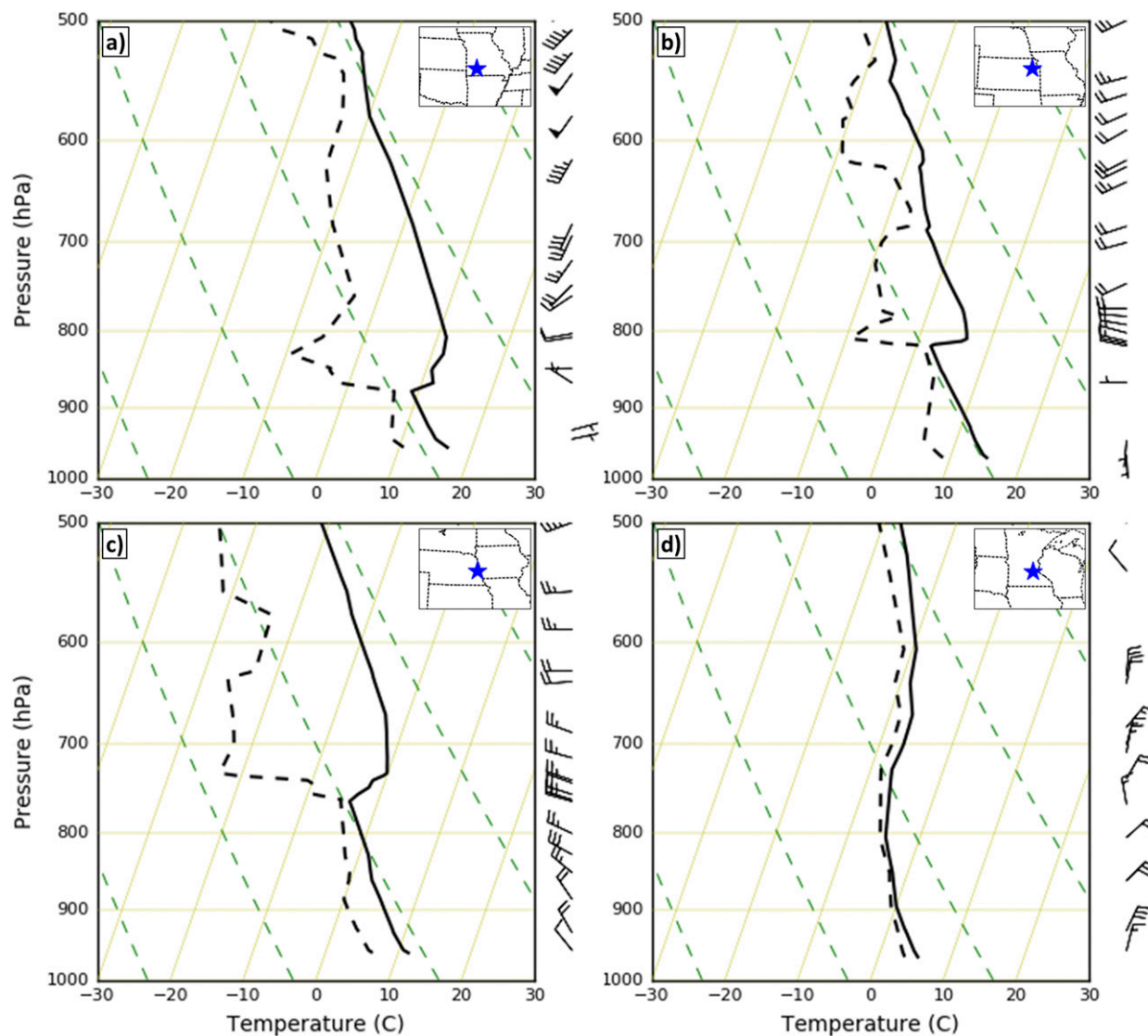
FIG. 9. As in Fig. 6, but at 0000 UTC 27 Apr 2011 at (a) Springfield, Missouri; (b) Topeka, Kansas; (c) Omaha, Nebraska; and (d) Chanhassen, Minnesota. Soundings are plotted up to 500 hPa without hypothetical parcel paths.

encompass an area exceeding $10\,000\,\mathrm{km}^2$ at one point during their lifetime. Table 1 provides a monthly summary of the 627 detected features identified during 1 March–31 August 2011. June is the most active month for mesoscale features over the TA domain, with 156 features detected (24.9%). April, May, and August are also active, with July (12.0%) and March (5.4%) exhibiting the fewest features across the TA domain. Roughly equal numbers of positive and negative pressure perturbations are identified.

Table 2 focuses on the 450 (71.8% of the total in Table 1) features that exhibited a peak pressure perturbation magnitude of 3 hPa or were accompanied by high winds nearby (within 50 km and within 30 min of feature passage)

as reported in the National Climatic Data Center (NCDC) publication *Storm Data*. While *Storm Data* wind and damage reports can be problematic (Trapp et al. 2006; Smith et al. 2013), the reports have been heavily used in previous works to assist in identification and classification of severe weather events (e.g., Coniglio et al. 2004; Ashley and Mote 2005). As shown in Table 2, 206 features were characterized by large pressure perturbations and high winds at some point during their lifetime, while 156 (88) features exhibited large pressure perturbations (high winds) only. These potentially high-impact events were each reviewed subjectively using radar imagery, surface observations, and gridded surface and upper air analysis fields. Not surprisingly,
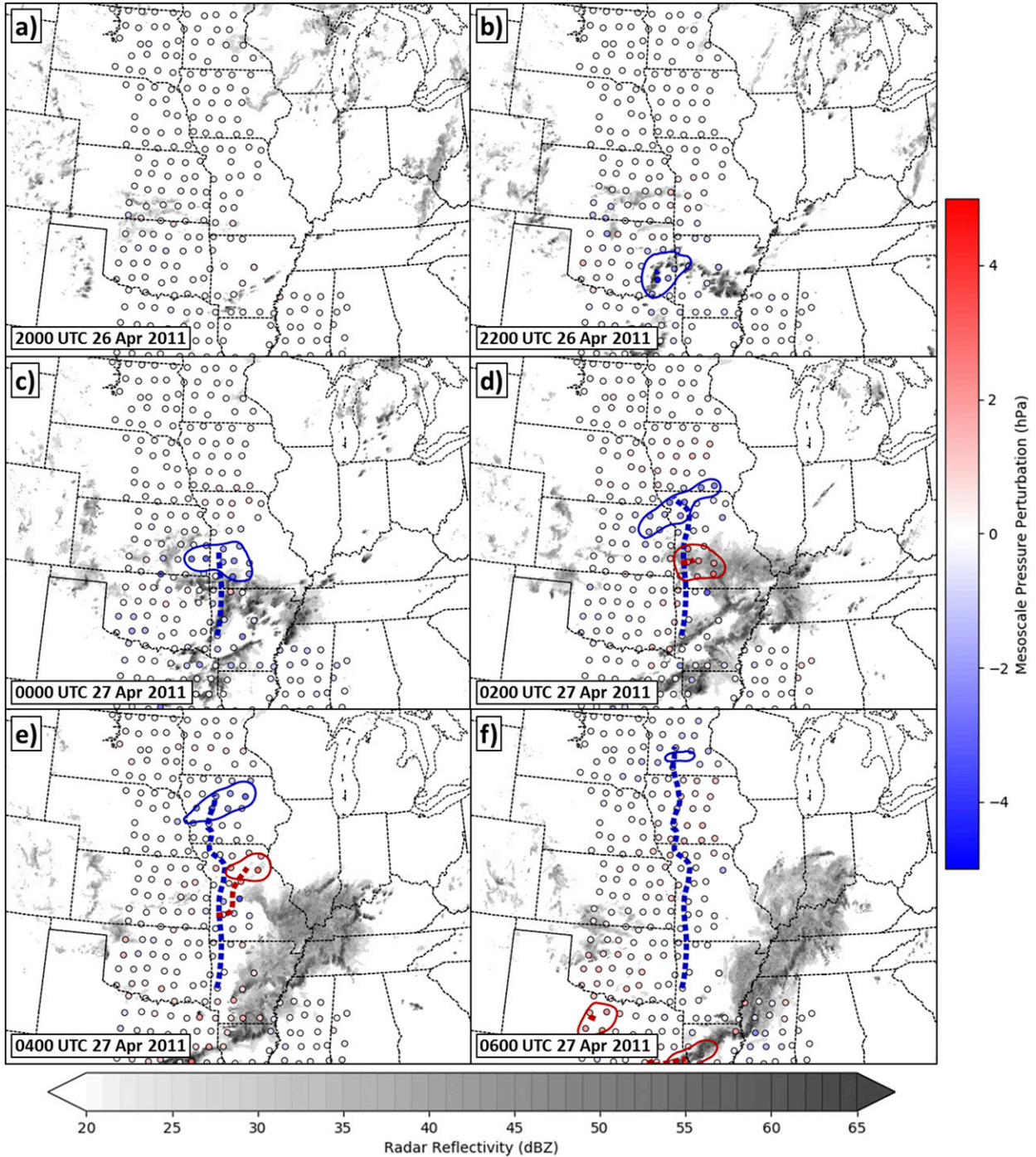
FIG. 10. As in Fig. 7, but at (a) 2000 UTC 26 Apr 2011, (b) 2200 UTC 26 Apr 2011, (c) 0000 UTC 27 Apr 2011, (d) 0200 UTC 27 Apr 2011, (e) 0400 UTC 27 Apr 2011, and (f) 0600 UTC 27 Apr 2011 across the central CONUS.

precipitation fell in the vicinity of nearly all (98%) of these perturbation features. Roughly half (239) of the features exhibited MCS signatures (e.g., mesohighs or wake lows) while 30% (137) could be characterized as being associated with multicellular or disorganized

convection. A smaller set of cases were associated with convection along frontal boundaries while only five events (including the case examined in section 3c) appeared to result from gravity waves with no substantial convection nearby. It is known that convection and
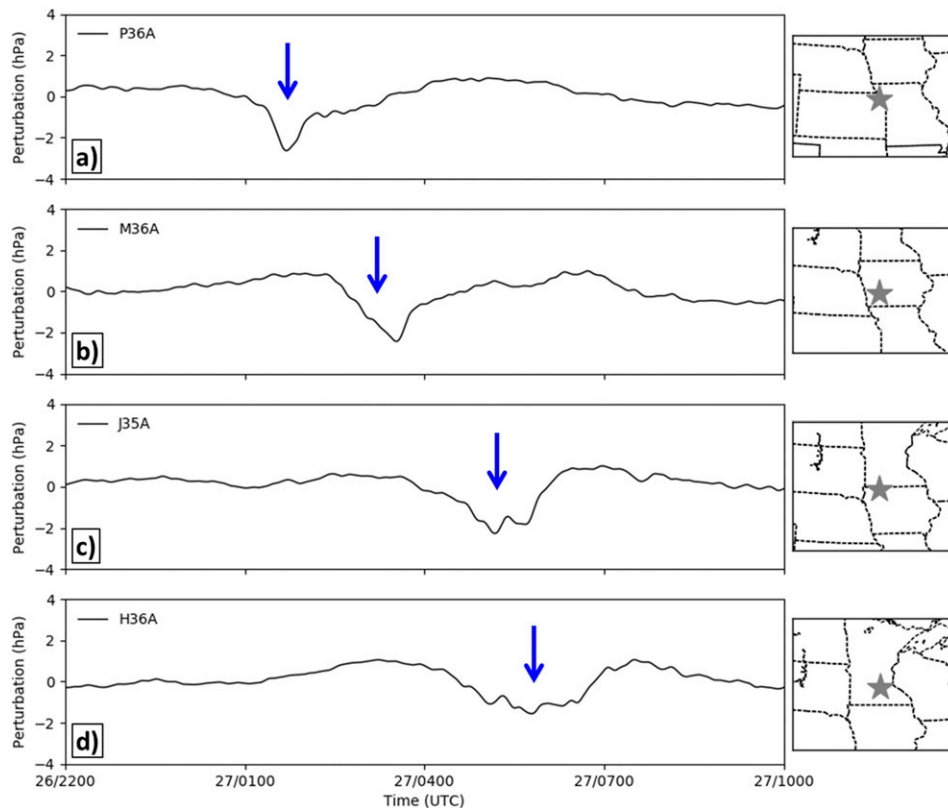
FIG. 11. As in Fig. 8, but valid at 2200 UTC 26 Apr 2011–1000 UTC 27 Apr 2011 at TA stations (a) P36A, (b) M36A, (c) J35A, and (d) H36A. The negative pressure perturbation associated with the gravity wave is depicted by a blue arrow.

mesoscale gravity waves can be collocated frequently (e.g., Ruppert and Bosart 2014), therefore, some of the assessed multicellular or disorganized convection cases could be related to mesoscale gravity waves.

Figure 12 highlights the locations of the unique pressure features detected during spring and summer 2011. The majority of events during spring 2011 are concentrated across the central and southern Great Plains with more events and the center of action shifting northward during summer. Figure 13 illustrates the tracks for all positive (red) and negative (blue) pressure perturbation features. Most features progress from southwest to northeast across the assessed domain during April and May (Figs. 13b,c). Since synoptic-scale southwest flow is often present across this region during that time of year,

mid- to late-spring convection often initiates in the warm sector of synoptic systems and moves east to northeast along or near established baroclinic zones. Mesoscale and inertial gravity wave events also have typically similar propagation patterns given their preferred area of genesis relative to synoptic systems (e.g., Koppel et al. 2000). In contrast, a shift to the north and change in orientation of the tracks is evident from July to August (Figs. 13e,f). Clear northwest–southeast patterns are seen in August, providing evidence that events similar to the 11–12 August 2011 MCS cases dominate this portion of the study period. The average track standard deviation for the features shown in Fig. 13 is 35°. Through the subjective analyses conducted above (Table 2), the larger track variations (bends and shifts)

TABLE 1. Counts (percentages) of prominent mesoscale pressure perturbation features detected during 1 Mar–31 Aug 2011 over the TA domain. Percentages for all features are relative to the total number (627) while percentages for positive and negative ones are relative to the total during that month.

Description	Mar	Apr	May	Jun	Jul	Aug	Total
Positive	12 (35)	54 (45)	61 (52)	78 (50)	43 (57)	65 (52)	313 (50)
Negative	22 (65)	65 (55)	56 (48)	78 (50)	32 (43)	61 (48)	314 (50)
All	34 (5)	119 (19)	117 (19)	156 (25)	75 (12)	126 (20)	627 (100)

TABLE 2. Counts (percentages) of high-impact mesoscale pressure perturbation features, defined as having perturbation magnitudes exceeding 3 hPa or near *Storm Data* high wind reports. The features are categorized subjectively as discussed in the text.

Category	Feature count (%)
Perturbation magnitude ≥3 hPa and associated with high winds	206 (45.8)
Perturbation magnitude ≥3 hPa only	156 (34.7)
Perturbation only associated with high winds	88 (19.5)
Total	450 (100.0)
Precipitation	439 (97.6)
No precipitation	11 (2.4)
Total	450 (100.0)
MCS (mesohigh–wake low)	239 (53.1)
Other convective features	137 (30.4)
Frontal systems	68 (15.1)
Gravity wave–type features without persistent convection	5 (1.1)
Not classifiable	1 (0.3)
Total	450 (100.0)

are primarily due to perturbation areal increase (decrease) with convective development (decay).

b. Feature characteristics

Figure 14a summarizes the lifetime of detected features during the 1 March–31 August 2011 period within our analysis domain. Most of the features last less than 3 h (72.9%), with 21.4% of them lasting from 3 to 6 h. Long-lived MCS events moving across the TA domain such as the two case studies examined earlier are relatively rare, with the gravity wave lasting 7.4 h (97th percentile) and the mesohigh of the primary MCS lasting 10.1 h (99th percentile).

Figure 14b illustrates the maximum areal extent of the detected features. As anticipated, features with smaller areal extent are more common, with 70.5% less than $40\,000\,\text{km}^2$ and only 5.3% larger than $80\,000\,\text{km}^2$ during their lifetime. Summarizing the total distance traveled by the features (Fig. 14c), most moved less than 200 km. The distance traveled is calculated by assessing the movement of the feature every 5 min. The combination of a shorter life span (Fig. 14a) and small propagation velocity is in part responsible for the majority moving less than 200 km. Very few events (5.3%) propagate farther than 500 km, many of which correspond with features with longer duration periods (not shown). An extreme case for this period was the 26–27 April 2011 gravity wave, which moved 1140 km away from its generation point, the maximum distance assessed for any feature in this study. In terms of feature perturbation strength, distributions for both positive and negative features are generally similar, with many features having a maximum observed perturbation magnitude of 2–4 hPa (not shown).

c. Feature speeds and directions

The distributions of median speed and direction for all assessed mesoscale features are provided in Fig. 15. Consistent with phase speeds noted in the literature, 76.1% of the features have a median speed between 15 and $35\,\text{m}\,\text{s}^{-1}$. Features with median speeds less than $15\,\text{m}\,\text{s}^{-1}$ ($>35\,\text{m}\,\text{s}^{-1}$) compose 11.2% (12.7%) of the total. A general eastward progression of the features is also evident (Fig. 15b), with most features moving in a general eastward to southeastward direction, with northeasterly movement a secondary maximum. Few features have a median northwesterly direction of motion over their life span during this period.

Since the speed and direction of features vary within their life span, those parameters are binned within geographic sectors over the TA domain for each 5-min period during the features' lifetime. Figure 16 shows the resulting normalized feature speed and direction roses for each sector over the 6-month period (note that features that last longer or remain in a particular sector may be weighted more heavily in these roses). Speeds of $15–35\,\text{m}\,\text{s}^{-1}$ occur most frequently in all sectors and for all movement directions. Features in the northeast sector of the TA domain appear to favor propagation directions that are northeasterly to easterly, whereas an easterly to southeasterly propagation direction is favored farther west and south.

The results presented in Fig. 16 are divided into the two seasons in Fig. 17. As expected from the monthly feature tracks (Fig. 13), shifts in preferred directions are seen between the two seasons in all sectors, with east-northeast movement preferred in spring and east-southeast movement during summer. In addition to an overall decrease in speed from spring to summer, fewer features travel faster than $35\,\text{m}\,\text{s}^{-1}$ at some point during their lifetime in summer compared to spring. This result likely follows from weaker synoptic mid- to upper-level flow during summer, with mesoscale processes dominating at that time across the Great Plains. Slight differences were found between the speed and direction of positive and negative pressure perturbation features during the period of study (not shown). A slight tendency was found for positive perturbations to favor east to southeast directions while negative perturbations favor east to northeast movement.

5. Summary and discussion

Mesoscale pressure perturbation features, many of which were associated with high-impact sensible weather, were assessed during the 1 March–31 August 2011 period across the central CONUS. Two distinct resources of
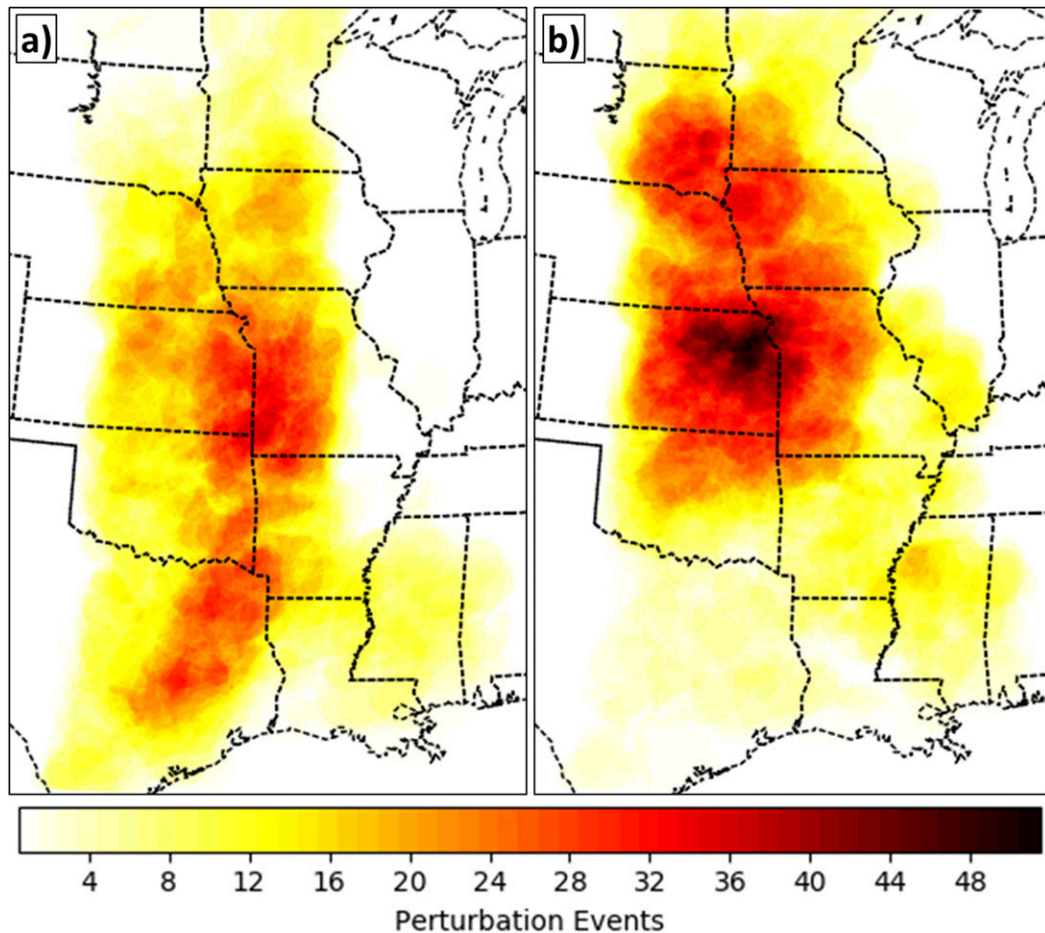
FIG. 12. Pressure perturbation features as a function of location during (a) spring (MAM) 2011 and (b) summer (JJA) 2011. Values are expressed as number of unique features assessed at each 5-km horizontal grid cell within the region encompassed by the TA (Fig. 1) during those periods.

surface pressure information were combined into surface pressure analyses at 5-km resolution every 5 min during the period of interest: 1) hourly RTMA surface pressure analyses at 5-km resolution and 2) pressure observations at 1-Hz temporal resolution and ~70-km spacing from sensors deployed as part of the USArray TA seismic field campaign, which was located across the central CONUS during the study period (Fig. 1). Temporal bandpass filtering (10 min–12 h) of the pressure analyses helped to detect perturbations produced by prominent mesoscale phenomena. A perturbation feature tracking algorithm was used to isolate large ($\geq 10\,000\,\text{km}^2$) and long-lived (>1 h) mesoscale perturbation features and evaluate their characteristics over time (e.g., propagation speed and direction).

The deployment strategy of the TA restricted the location, temporal period, and scale of the phenomena that could be examined for this study. Although large-magnitude inertial gravity waves occur occasionally from the Great Lakes eastward (Bosart et al. 1998;

Koppel et al. 2000), the overall frequency of mesoscale pressure perturbations observed decreased as the TA migrated eastward after August 2011 (Jacques et al. 2015). Mesoscale pressure perturbations that lasted an hour or more were assessed due to the coarse spatial separation (~70 km) between TA sites and the coarse hourly resolution and apparent errors on the mesoscale of the RTMA background fields.

The two case studies in section 3 illustrate the analysis approach applied to different mesoscale phenomena. The 11–12 August 2011 MCS features (Figs. 7–8) highlight the ability to detect and track mature, large-scale mesohighs and wake lows. While others have often focused on identifying and tracking feature boundaries to assess feature propagation (e.g., Ruppert and Bosart 2014), the perturbations associated with the first MCS highlight how the evolving nature of a large MCS can leads to shifts and variations in its speed and direction (Fig. 7). Although the 26–27 April 2011 gravity wave
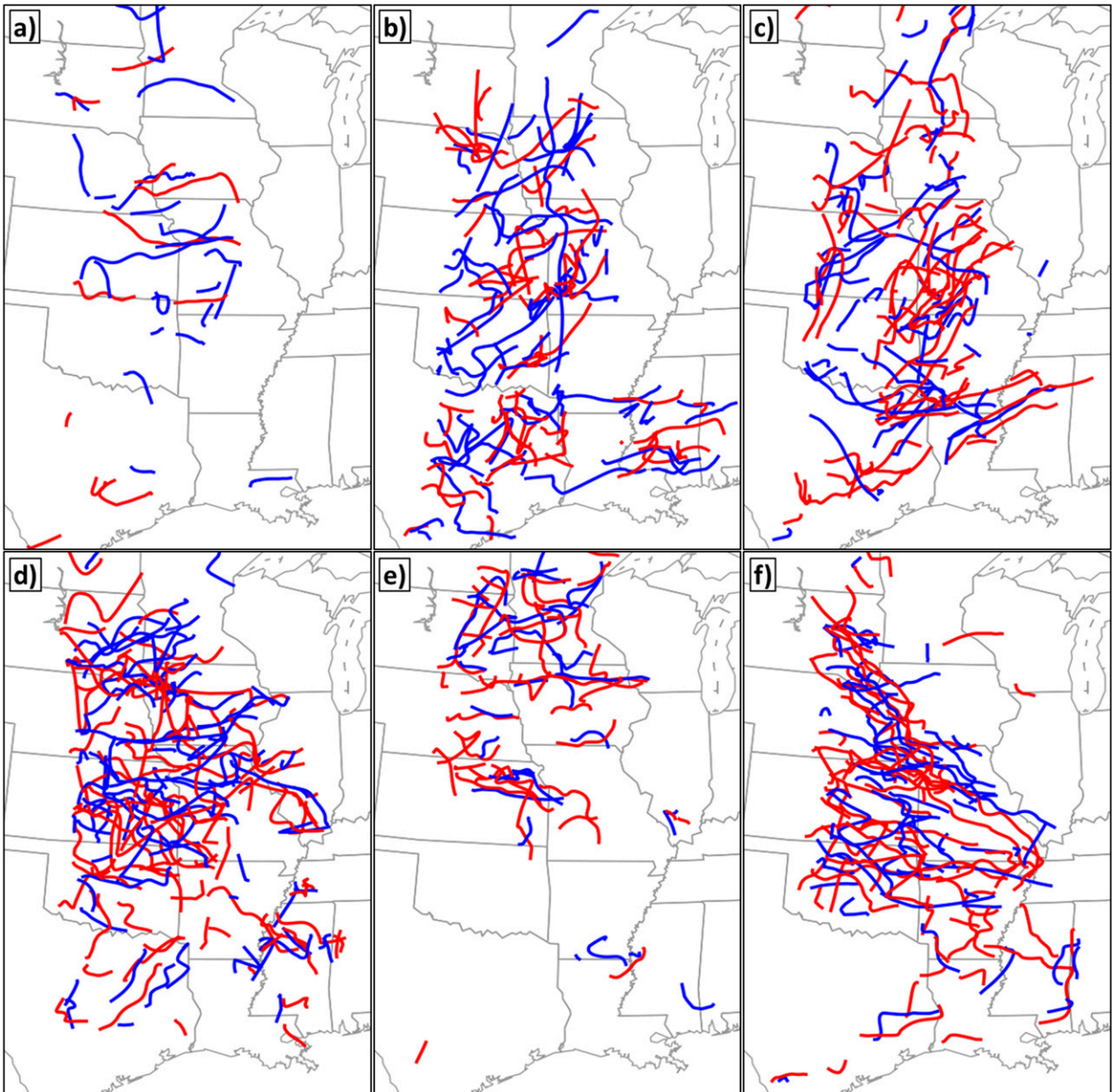
FIG. 13. Feature tracks for positive (red) and negative (blue) pressure perturbations during (a) March, (b) April, (c) May, (d) June, (e) July, and (f) August 2011.

case (Figs. 10–11) illustrates the tracking of a coherent mesoscale feature over long distances and time periods, it is entirely fortuitous that this gravity wave propagated from south to north through the TA. Other waves traveling across the shorter east–west dimension of the TA could only be tracked for shorter durations. While this event did not lead to wind damage, the enhancement and relaxation of wind speeds during and after its passage may have been important for wind energy applications in the region since wind ramp events are often difficult to identify in advance.

The aggregate statistics (section 4) for the detected features are consistent with reviews of mesoscale phenomena occurrences (Koppel et al. 2000; Bentley et al. 2000; Guastini and Bosart 2016) and specific case studies (Bosart and Seimon 1988; Schneider 1990; Bosart et al. 1998; Ruppert and Bosart 2014). The Eulerian approach used by Jacques et al. (2015) is extended here using a more Lagrangian perspective. Table 1 and Figs. 12 and 13 highlight that, within the TA domain during the spring and summer of 2011, mesoscale features were most frequent across the central Great Plains region of
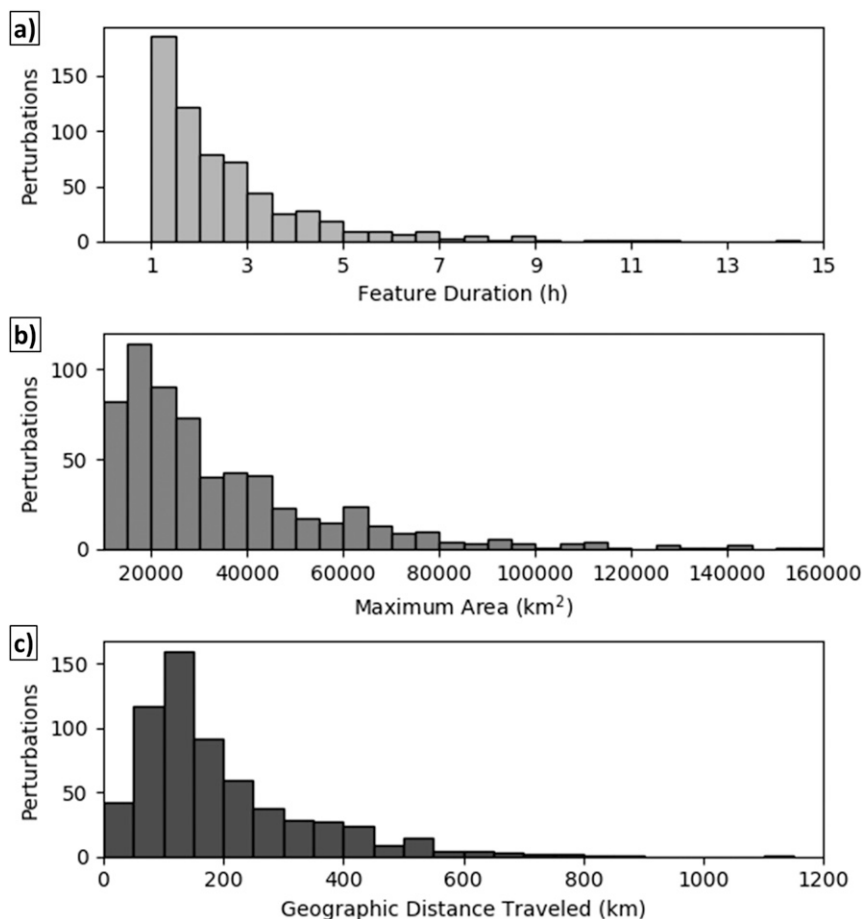
FIG. 14. Perturbation features summarized by (a) duration (h), (b) maximum 1-hPa perturbation areal extent (km²), and (c) geographic distance traveled (km).

the CONUS. Table 2 shows that nearly all of the high-impact mesoscale pressure features for the period studied were associated with precipitation and convective processes. Spring convection with east-northeastward gravity wave propagation transitioned to summer easterly and southeasterly propagating MCS events as the jet stream shifted north and ridging dominated the southern Great Plains. The majority of the features that we were able to detect have brief life spans (less than 3 h), small areal extent (less than 40 000 km²), and short propagation distances (less than 200 km). As expected, the case studies shown in section 3 are more extreme cases. The histograms of median propagation speeds (Fig. 15a) place over 76% of the detected features within 15–35 m s⁻¹. Wind roses computed from speeds and directions evaluated within the features' lifetime support previous work describing general speed and direction characteristics for MCS, derecho, and large-magnitude gravity wave phenomena (Bosart et al. 1998; Koppel et al. 2000; Adams-Selin and Johnson 2013).

There has been considerable interest over the years to automate real-time gravity wave detection via time–space transform techniques (e.g., Koch and O'Handley 1997; Koch and Saleeby 2001). However, those studies highlighted issues during that era associated with acquiring real-time observations with adequate temporal resolution as well as the data assimilation procedures, time, and computer resources required to process and detect mesoscale features. Those limitations have largely been resolved today. While our research relies on field campaign data that by itself is not practical for operational applications (due to the short-term existence of the TA stations and the relatively restricted geographic domain), Fig. 18 illustrates the coverage available now from publicly accessible high-frequency (≤15 min) pressure observations across the CONUS from Mesowest (Horel et al. 2002). As a simple metric ignoring differences in observation quality from the various sources, Fig. 18 shows the minimum distance from each 5-km RTMA grid point to the nearest
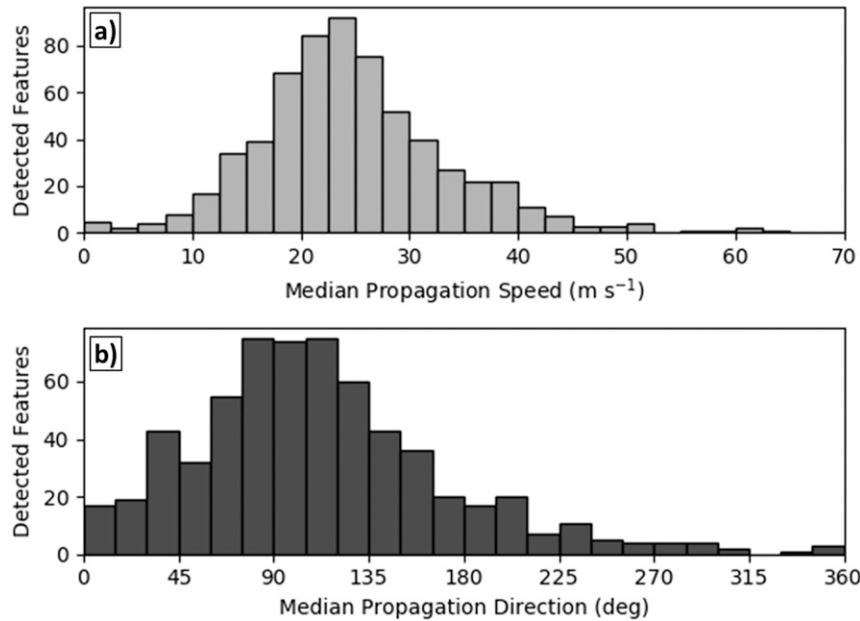
FIG. 15. As in Fig. 14, but summarized in terms of (a) median speed and (b) median direction.

pressure sensor location. The median distance is 29.5 km, well below the ~70-km spacing available from the TA sites used in this study. The eastern CONUS and urban areas are covered quite well with most locations within 25 km of a pressure observation; however, locations across the intermountain western CONUS often exceed 100–150 km. Figure 18 should be considered a conservative estimate of station spacing as many government and commercial networks with pressure sensors restrict public access but are available to NCEP operations (e.g., Oklahoma and New York Mesonets, EarthNetworks). In addition, considerable potential may result from harnessing the vast number of pressure sensors in smartphones (Mass and Madaus 2014).

The abundance of observations suggests that it could be possible to create a robust multiyear climatology of mesoscale pressure features across regions where MCS and gravity waves are prevalent. This methodology could also be quite useful for case analyses of specific events for a variety of applications. For example, more in-depth detection analysis of perturbations related to solitary gravity wave propagation could be useful for the wind energy industry to assist with wind ramp forecasting. To take advantage of observational resources for applications such as the above, improved quality control procedures and metadata are clearly needed. For example, a large fraction of the pressure data used to generate Fig. 18 are available from the Citizen Weather Observing

Program (CWOP), which in some instances may have inaccurate station metadata (e.g., a CWOP member may incorrectly input their elevation in feet instead of meters or the location of the site may be in error). Any future gravity wave tracking system should rely on other surface
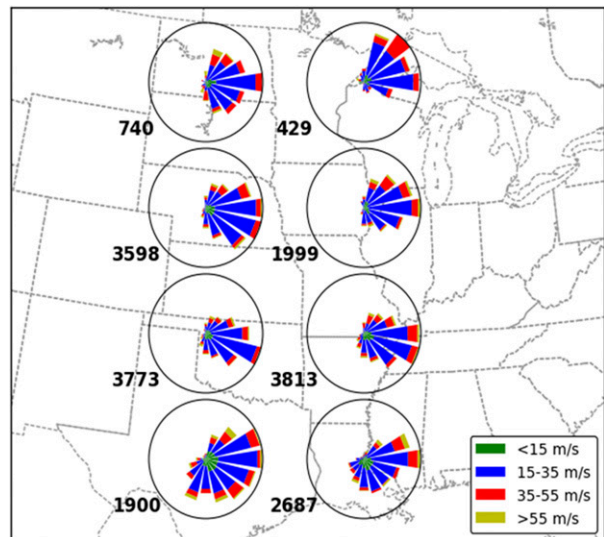

FIG. 16. Feature speed and direction roses for all features detected during 1 Mar–31 Aug 2011. Features are split into eight geographic sectors as shown by the rose locations, with total sample counts to the lower left of each sector. Samples are derived from the speeds and directions every 5 min during every features' lifetime.
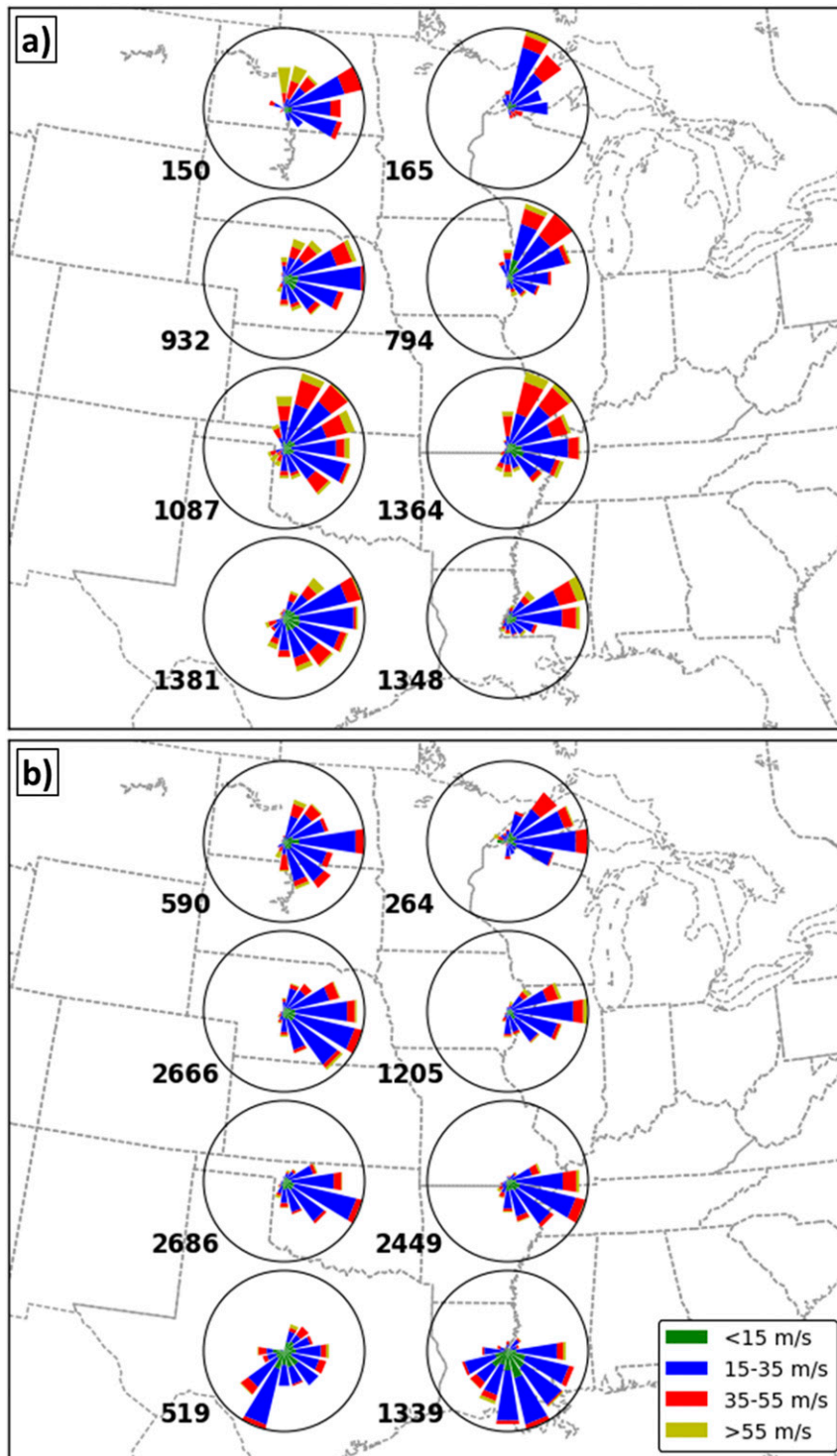
FIG. 17. As in Fig. 16, but divided into features during (a) spring (MAM) and (b) summer (JJA).

sensors (e.g., precipitation, temperature, moisture, and wind) as well as upper air observing capabilities from radiosondes, surface-based remote sensors, and satellite. Although there are, for example, more surface wind observations when including mesonet data, quality control of surface observations becomes even more important for parameters other than pressure as sensor siting can lead to large representativeness issues in urban,
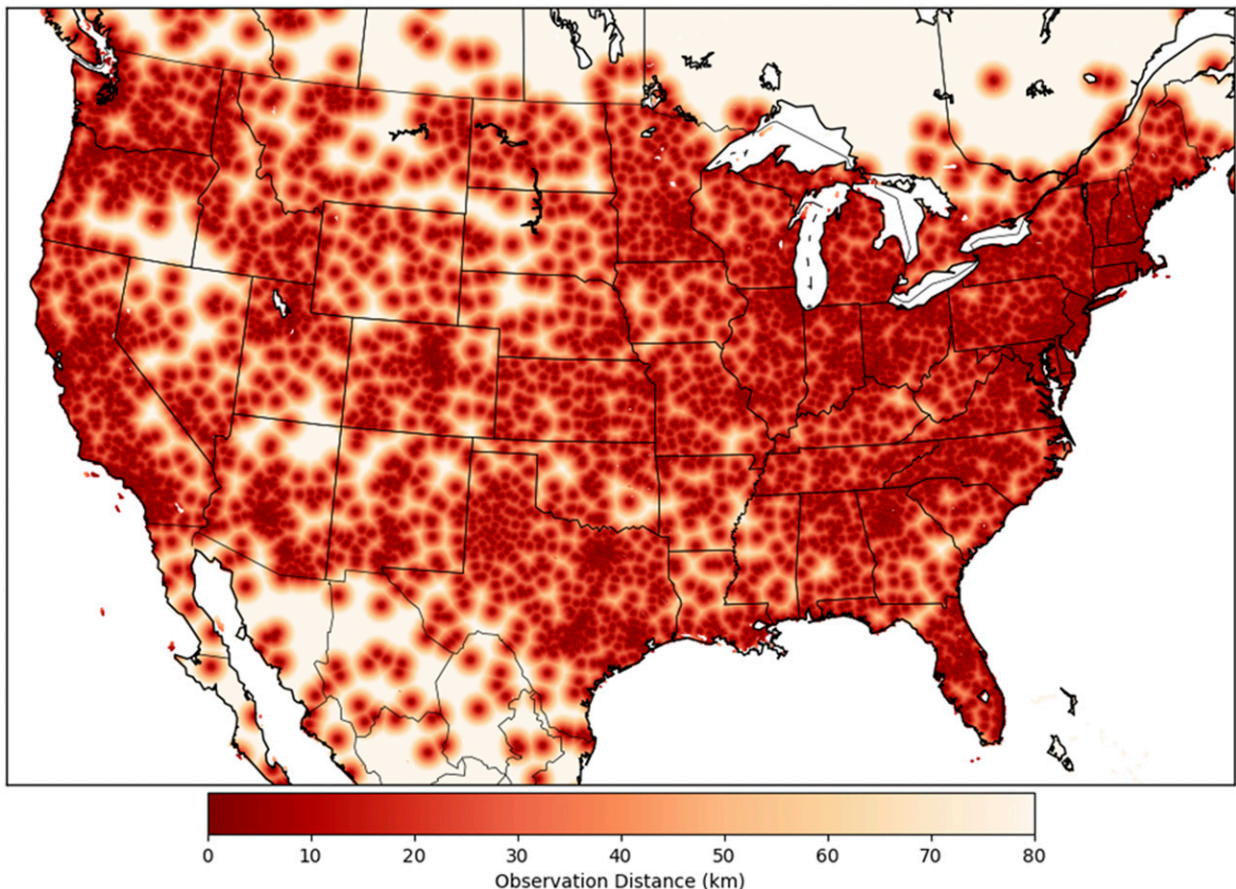
FIG. 18. Distribution of the minimum distance between a location and the nearest high-frequency (≤15 min) pressure observation publicly available via Mesowest on 15 Nov 2016. Darker colors represent locations close to mesonet stations reporting pressure, while lighter colors represent farther distances. Oceanic regions are not considered for this figure.

mountainous, forested, and coastal regions of the country (Tyndall and Horel 2013).

To take full advantage of the high-resolution data now available, improved data assimilation methods are required that assimilate those observations, retain gravity wave features that often induce numerical instabilities in current models, and provide guidance at high temporal and spatial resolution. Such improvements could be fostered through numerical modeling and data assimilation of past events or idealized phenomena (e.g., MCS or large-magnitude solitary gravity waves). Further improvements to the now 2.5-km resolution RTMA are likely to continue, although its output frequency remains hourly. Operational and experimental versions of the High-Resolution Rapid Refresh (HRRR) data assimilation and forecast system (that now serve as the background fields for the RTMA) provide some output wind fields at 15 min (Benjamin et al. 2016). The algorithms and results presented here highlight the potential for further research and development of algorithms applied to such numerical guidance to detect mesoscale features that can, directly or indirectly, impact lives, property, and industry.

REFERENCES

Achatz, U., B. Ribstein, F. Senf, and R. Klein, 2017: The interaction between synoptic-scale balanced flow and a finite-amplitude mesoscale wave field throughout all atmospheric layers: Weak and moderately strong stratification. *Quart. J. Roy. Meteor. Soc.*, **143**, 342–361, doi:10.1002/qj.2926.

Adams-Selin, R. D., and R. H. Johnson, 2010: Mesoscale surface pressure and temperature features associated with bow echoes. *Mon. Wea. Rev.*, **138**, 212–227, doi:10.1175/2009MWR2892.1.

——, and ——, 2013: Examination of gravity waves associated with the 13 March 2003 bow echo. *Mon. Wea. Rev.*, **141**, 3735–3756, doi:10.1175/MWR-D-12-00343.1.

Anderson, J. L., B. Wyman, S. Zhang, and T. Hoar, 2005: Assimilation of PS observations using an ensemble filter in an idealized global atmospheric prediction system. *J. Atmos. Sci.*, **62**, 2925–2938, doi:10.1175/JAS3510.1.

Ashley, W. S., and T. L. Mote, 2005: Derecho hazards in the United States. *Bull. Amer. Meteor. Soc.*, **86**, 1577–1592, doi:10.1175/BAMS-86-11-1577.

Benjamin, S. G., J. M. Brown, G. Manikin, and G. Mann, 2007: The RTMA background—Hourly downscaling of RUC data to 5-km detail. *22nd Conf. on Weather Analysis and Forecasting/18th Conf. on Numerical Weather Prediction*, Park City, UT, Amer. Meteor. Soc., 4A.6. [Available online at http://ams.confex.com/ams/pdfpapers/124825.pdf.]

——, and Coauthors, 2016: A North American hourly assimilation and model forecast cycle: The Rapid Refresh. *Mon. Wea. Rev.*, **144**, 1669–1694, doi:10.1175/MWR-D-15-0242.1.

Bentley, M. L., T. L. Mote, and S. F. Byrd, 2000: A synoptic climatology of derecho producing mesoscale convective systems in the north-central Plains. *Int. J. Climatol.*, **20**, 1329–1349, doi:10.1002/1097-0088(200009)20:11<1329::AID-JOC537>3.0.CO;2-F.

Bosart, L. F., and A. Seimon, 1988: A case study of an unusually intense atmospheric gravity wave. *Mon. Wea. Rev.*, **116**, 1857–1886, doi:10.1175/1520-0493(1988)116<1857:ACSOAU>2.0.CO;2.

——, W. E. Bracken, and A. Seimon, 1998: A study of cyclone mesoscale structure with emphasis on a large-amplitude inertia–gravity wave. *Mon. Wea. Rev.*, **126**, 1497–1527, doi:10.1175/1520-0493(1998)126<1497:ASOCMS>2.0.CO;2.

Brown, R. A., and V. T. Wood, 2012: The tornadic vortex signature: An update. *Wea. Forecasting*, **27**, 525–530, doi:10.1175/WAF-D-11-00111.1.

Bullock, R., 2011: Development and implementation of MODE time domain object-based verification. *24th Conf. on Weather and Forecasting/20th Conf. on Numerical Weather Prediction*, Seattle, WA, Amer. Meteor. Soc., 96. [Available online at https://ams.confex.com/ams/91Annual/webprogram/Paper182677.html.]

Centurioni, L., A. Horányi, C. Cardinali, E. Charpentier, and R. Lumpkin, 2017: A global ocean observing system for measuring sea level atmospheric pressure: Effects and impacts on numerical weather prediction. *Bull. Amer. Meteor. Soc.*, **98**, 231–238, doi:10.1175/BAMS-D-15-00080.1.

Clark, A. J., R. G. Bullock, T. L. Jensen, M. Xue, and F. Kong, 2014: Application of object-based time-domain diagnostics for tracking precipitation systems in convection-allowing models. *Wea. Forecasting*, **29**, 517–542, doi:10.1175/WAF-D-13-00098.1.

Coleman, T. A., and K. R. Knupp, 2009: Factors affecting surface wind speeds in gravity waves and wake lows. *Wea. Forecasting*, **24**, 1664–1679, doi:10.1175/2009WAF2222248.1.

Compo, G. P., J. S. Whitaker, and P. D. Sardeshmukh, 2006: Feasibility of a 100-year reanalysis using only surface pressure data. *Bull. Amer. Meteor. Soc.*, **87**, 175–190, doi:10.1175/BAMS-87-2-175.

——, and Coauthors, 2011: The Twentieth Century Reanalysis Project. *Quart. J. Roy. Meteor. Soc.*, **137**, 1–28, doi:10.1002/qj.776.

Coniglio, M. C., D. J. Stensrud, and M. B. Richman, 2004: An observational study of derecho-producing convective systems. *Wea. Forecasting*, **19**, 320–337, doi:10.1175/1520-0434(2004)019<0320:AOSODC>2.0.CO;2.

——, S. F. Corfidi, and J. S. Kain, 2011: Environment and early evolution of the 8 May 2009 derecho-producing convective system. *Mon. Wea. Rev.*, **139**, 1083–1102, doi:10.1175/2010MWR3413.1.

Crook, N. A., 1988: Trapping of low-level internal gravity waves. *J. Atmos. Sci.*, **45**, 1533–1541, doi:10.1175/1520-0469(1988)045<1533:TOLLIG>2.0.CO;2.

Davis, C. A., B. Brown, and R. Bullock, 2006: Object-based verification of precipitation forecasts. Part I: Methodology and application to mesoscale rain areas. *Mon. Wea. Rev.*, **134**, 1772–1784, doi:10.1175/MWR3145.1.

——, ——, ——, and J. Halley-Gotway, 2009: The Method for Object-Based Diagnostic Evaluation (MODE) applied to numerical forecasts from the 2005 NSSL/SPC Spring Program. *Wea. Forecasting*, **24**, 1252–1267, doi:10.1175/2009WAF2222241.1.

de Groot-Hedlin, C. D., M. A. H. Hedlin, K. Walker, D. P. Drob, and M. Zumberge, 2008: Study of propagation from the shuttle Atlantis using a large seismic network. *J. Acoust. Soc. Amer.*, **124**, 1442–1451, doi:10.1121/1.2956475.

——, ——, and K. T. Walker, 2014: Detection of gravity waves across the USArray: A case study. *Earth Planet. Sci. Lett.*, **402**, 346–352, doi:10.1016/j.epsl.2013.06.042.

de Pondeca, M., and Coauthors, 2011: The Real-Time Mesoscale Analysis at NOAA's National Centers for Environmental Prediction: Current status and development. *Wea. Forecasting*, **26**, 593–612, doi:10.1175/WAF-D-10-05037.1.

Engerer, N. A., D. J. Stensrud, and M. C. Coniglio, 2008: Surface characteristics of observed cold pools. *Mon. Wea. Rev.*, **136**, 4839–4849, doi:10.1175/2008MWR2528.1.

Evans, J. S., and C. A. Doswell III, 2001: Examination of derecho environments using proximity soundings. *Wea. Forecasting*, **16**, 329–342, doi:10.1175/1520-0434(2001)016<0329:EODEUP>2.0.CO;2.

Galarneau, T. J., Jr., L. F. Bosart, C. A. Davis, and R. McTaggart-Cowan, 2009: Baroclinic transition of a long-lived mesoscale convective vortex. *Mon. Wea. Rev.*, **137**, 562–584, doi:10.1175/2008MWR2651.1.

Grivet-Talocia, S., and F. Einaudi, 1998: Wavelet analysis of a microbarograph network. *IEEE Trans. Geosci. Remote Sens.*, **36**, 418–433, doi:10.1109/36.662727.

——, ——, W. L. Clark, R. D. Dennett, G. D. Nastrom, and T. E. VanZandt, 1999: A 4-yr climatology of pressure disturbances using a barometer network in central Illinois. *Mon. Wea. Rev.*, **127**, 1613–1629, doi:10.1175/1520-0493(1999)127<1613:AYCOPD>2.0.CO;2.

Guastini, C. T., and L. F. Bosart, 2016: Analysis of a progressive derecho climatology and associated formation environments. *Mon. Wea. Rev.*, **144**, 1363–1382, doi:10.1175/MWR-D-15-0256.1.

Hedlin, M. A. H., D. Drob, K. Walker, and C. D. de Groot-Hedlin, 2010: A study of acoustic propagation from a large bolide in the atmosphere with a dense seismic network. *J. Geophys. Res.*, **115**, B11312, doi:10.1029/2010JB007669.

——, C. D. de Groot-Hedlin, and D. P. Drob, 2012: A study of infrasound propagation using dense seismic network recordings of surface explosions. *Bull. Seismol. Soc. Amer.*, **102**, 1927–1937, doi:10.1785/0120110300.

Hodges, K. I., 1994: A general method for tracking analysis and its application to meteorological data. *Mon. Wea. Rev.*, **122**, 2573–2586, doi:10.1175/1520-0493(1994)122<2573:AGMFTA>2.0.CO;2.

——, B. J. Hoskins, J. Boyle, and C. Thorncroft, 2003: A comparison of recent reanalysis datasets using objective feature tracking: Storm tracks and tropical easterly waves. *Mon. Wea. Rev.*, **131**, 2012–2037, doi:10.1175/1520-0493(2003)131<2012:ACORRD>2.0.CO;2.

Horel, J., and Coauthors, 2002: Mesowest: Cooperative mesonets in the western United States. *Bull. Amer. Meteor. Soc.*, **83**, 211–225, doi:10.1175/1520-0477(2002)083<0211:MCMITW>2.3.CO;2.

Hoskins, B. J., and K. I. Hodges, 2002: New perspectives on the Northern Hemisphere winter storm tracks. *J. Atmos. Sci.*, **59**, 1041–1061, doi:10.1175/1520-0469(2002)059<1041:NPOTNH>2.0.CO;2.

Ingleby, B., 2015: Global assimilation of air temperature, humidity, wind and pressure from surface stations. *Quart. J. Roy. Meteor. Soc.*, **141**, 504–517, doi:10.1002/qj.2372.

Jacques, A. A., J. D. Horel, E. T. Crosman, and F. L. Vernon, 2015: Central and eastern U.S. surface pressure variations derived from the USArray network. *Mon. Wea. Rev.*, **143**, 1472–1493, doi:10.1175/MWR-D-14-00274.1.

——, ——, ——, ——, and J. Tytell, 2016: The Earthscope US Transportable Array 1 Hz surface pressure dataset. *Geosci. Data J.*, **3**, 29–36, doi:10.1002/gdj3.37.

Johnson, J. T., P. L. MacKeen, A. Witt, E. D. Mitchell, G. J. Stumpf, M. D. Eilts, and K. W. Thomas, 1998: The storm cell identification and tracking algorithm: An enhanced WSR-88D algorithm. *Wea. Forecasting*, **13**, 263–276, doi:10.1175/1520-0434(1998)013<0263:TSCIAT>2.0.CO;2.

Jung, S., and G. Lee, 2015: Radar-based cell tracking with fuzzy logic approach. *Meteor. Appl.*, **22**, 716–730, doi:10.1002/met.1509.

Knupp, K. R., and Coauthors, 2014: Meteorological overview of the devastating 27 April 2011 tornado outbreak. *Bull. Amer. Meteor. Soc.*, **95**, 1041–1062, doi:10.1175/BAMS-D-11-00229.1.

Koch, S. E., and C. O'Handley, 1997: Operational forecasting and detection of mesoscale gravity waves. *Wea. Forecasting*, **12**, 253–281, doi:10.1175/1520-0434(1997)012<0253:OFADOM>2.0.CO;2.

——, and S. Saleeby, 2001: An automated system for the analysis of gravity waves and other mesoscale phenomena. *Wea. Forecasting*, **16**, 661–679, doi:10.1175/1520-0434(2001)016<0661:AASFTA>2.0.CO;2.

König, W., R. Sausen, and F. Sielmann, 1993: Objective identification of cyclones in GCM simulations. *J. Climate*, **6**, 2217–2231, doi:10.1175/1520-0442(1993)006<2217:OIOCIG>2.0.CO;2.

Koppel, L. L., L. F. Bosart, and D. Keyser, 2000: A 25-yr climatology of large-amplitude hourly surface pressure changes over the conterminous United States. *Mon. Wea. Rev.*, **128**, 51–68, doi:10.1175/1520-0493(2000)128<0051:AYCOLA>2.0.CO;2.

Kravtsov, S., I. Rudeva, and S. K. Gulev, 2015: Reconstructing sea level pressure variability via a feature tracking approach. *J. Atmos. Sci.*, **72**, 487–506, doi:10.1175/JAS-D-14-0169.1.

Lei, L., and J. L. Anderson, 2014: Impacts of frequent assimilation of surface pressure observations on atmospheric analyses. *Mon. Wea. Rev.*, **142**, 4477–4483, doi:10.1175/MWR-D-14-00097.1.

Lindzen, R. S., and K. Tung, 1976: Banded convective activity and ducted gravity waves. *Mon. Wea. Rev.*, **104**, 1602–1617, doi:10.1175/1520-0493(1976)104<1602:BCAADG>2.0.CO;2.

Liu, Y., D.-G. Xi, Z.-L. Li, and C.-X. Shi, 2014: Automatic tracking and characterization of cumulonimbus clouds from FY-2C geostationary meteorological satellite images. *Adv. Meteor.*, **2014**, 478419, doi:10.1155/2014/478419.

Loehrer, S. M., and R. H. Johnson, 1995: Surface pressure and precipitation life cycle characteristics of PRE-STORM mesoscale convective systems. *Mon. Wea. Rev.*, **123**, 600–621, doi:10.1175/1520-0493(1995)123<0600:SPAPLC>2.0.CO;2.

Madaus, L. E., G. J. Hakim, and C. F. Mass, 2014: Utility of dense pressure observations for improving mesoscale analyses and forecasts. *Mon. Wea. Rev.*, **142**, 2398–2413, doi:10.1175/MWR-D-13-00269.1.

Mapes, B. E., 1993: Gregarious tropical convection. *J. Atmos. Sci.*, **50**, 2026–2037, doi:10.1175/1520-0469(1993)050<2026:GTC>2.0.CO;2.

Mass, C. F., and L. E. Madaus, 2014: Surface pressure observations from smartphones: A potential revolution for high-resolution weather prediction? *Bull. Amer. Meteor. Soc.*, **95**, 1343–1349, doi:10.1175/BAMS-D-13-00188.1.

McMillen, J. D., and W. J. Steenburgh, 2015: Capabilities and limitations of convection-permitting WRF simulations of lake-effect systems over the Great Salt Lake. *Wea. Forecasting*, **30**, 1711–1731, doi:10.1175/WAF-D-15-0017.1.

Metz, N. D., and L. F. Bosart, 2010: Derecho and MCS development, evolution, and multiscale interactions during 3–5 July 2003. *Mon. Wea. Rev.*, **138**, 3048–3070, doi:10.1175/2010MWR3218.1.

Mittermaier, M. P., and R. Bullock, 2013: Using MODE to explore the spatial and temporal characteristics of cloud cover forecasts from high-resolution NWP models. *Meteor. Appl.*, **20**, 187–196, doi:10.1002/met.1393.

Plougonven, R., and F. Zhang, 2014: Internal gravity waves from atmospheric jets and fronts. *Rev. Geophys.*, **52**, 33–76, doi:10.1002/2012RG000419.

Raible, C. C., P. M. Della-Marta, C. Schwierz, H. Wernli, and R. Blender, 2008: Northern Hemisphere extratropical cyclones: A comparison of detection and tracking methods and different reanalyses. *Mon. Wea. Rev.*, **136**, 880–897, doi:10.1175/2007MWR2143.1.

Ramamurthy, M. K., R. M. Rauber, B. P. Collins, and N. K. Malhotra, 1993: A comparative study of large-amplitude gravity-wave events. *Mon. Wea. Rev.*, **121**, 2951–2974, doi:10.1175/1520-0493(1993)121<2951:ACSOLA>2.0.CO;2.

Ruppert, J. H., and L. F. Bosart, 2014: A case study of the interaction of a mesoscale gravity wave with a mesoscale convective system. *Mon. Wea. Rev.*, **142**, 1403–1429, doi:10.1175/MWR-D-13-00274.1.

Schneider, R. S., 1990: Large-amplitude mesoscale wave disturbances within the intense Midwest extratropical cyclone of 15 December 1987. *Wea. Forecasting*, **5**, 533–558, doi:10.1175/1520-0434(1990)005<0533:LAMWDW>2.0.CO;2.

Smith, B. T., T. E. Castellanos, A. C. Winters, C. M. Mead, A. R. Dean, and R. L. Thompson, 2013: Measured severe convective wind climatology and associated convective modes of thunderstorms in the contiguous United States, 2003–09. *Wea. Forecasting*, **28**, 229–236, doi:10.1175/WAF-D-12-00096.1.

Trapp, R. J., D. M. Wheatley, N. T. Atkins, R. W. Przybylinski, and R. Wolf, 2006: Buyer beware: Some words of caution on the use of severe wind reports in postevent assessment

and research. *Wea. Forecasting*, **21**, 408–415, doi:10.1175/
WAF925.1.

Tyndall, D., and J. Horel, 2013: Impacts of mesonet observations
on meteorological surface analyses. *Wea. Forecasting*, **28**, 254–
269, doi:10.1175/WAF-D-12-00027.1.

Tytell, J., F. Vernon, M. Hedlin, C. de Groot Hedlin, J. Reyes,
B. Busby, K. Hafner, and J. Eakins, 2016: The USArray
Transportable Array as a platform for weather observation
and research. *Bull. Amer. Meteor. Soc.*, **97**, 603–619, doi:10.1175/
BAMS-D-14-00204.1.

Whitaker, J. S., G. P. Compo, X. Wei, and T. M. Hamill, 2004:
Reanalysis without radiosondes using ensemble data
assimilation. *Mon. Wea. Rev.*, **132**, 1190–1200, doi:10.1175/
1520-0493(2004)132<1190:RWRUED>2.0.CO;2.

Yussouf, N., D. C. Dowell, L. J. Wicker, K. H. Knopfmeier, and
D. M. Wheatley, 2015: Storm-scale data assimilation and en-
semble forecasts for the 27 April 2011 severe weather out-
break in Alabama. *Mon. Wea. Rev.*, **143**, 3044–3066, doi:10.1175/
MWR-D-14-00268.1.

Zhang, F., S. E. Koch, C. A. Davis, and M. L. Kaplan, 2001:
Wavelet analysis and the governing dynamics of a large-
amplitude mesoscale gravity-wave event along the East
Coast of the United States. *Quart. J. Roy. Meteor. Soc.*, **127**,
2209–2245, doi:10.1002/qj.49712757702.